A Device for the Graded Mechanostimulation of Cultured Neurons

A Thesis
Presented to
The Academic Faculty

By

Harrison Norman

In Partial Fulfillment
of the Requirements for the Degree
Master of Science in Bioengineering

Georgia Institute of Technology

December, 2014

A Device for the Mechanostimulation of Cultured Neurons

Approved by:

Dr. C. Ross Ethier, Advisor
Wallace H. Coulter Department of Biomedical Engineering
Georgia Institute of Technology

Dr. Robert Butera
School of Electrical and Computer Engineering
Georgia Institute of Technology

Dr. Machelle T. Pardue
Department of Ophthalmology
Emory University

Date Approved: December 2, 2014

To my grandmother, Marcella Martin Hilliard

ACKNOWLEDGMENTS

I would like to thank my advisor, Dr. C. Ross Ethier for his time, patience, and enthusiasm during my experience as a graduate student in his lab. I would also like to thank Dr. Machelle Pardue and her lab for teaching me the finer points of retinal function and physiology in lab meetings, and in the wonderful course: IBS 548: Biology of the Eye. Further, I would like to thank Dr. Robert Butera for serving on my committee, and allowing me the great opportunity to do a rotation in his lab during my first months at Tech.

I can't imagine that the cell work presented in this document would have been possible without the guidance and assistance of Dr. Lisa Schildmeyer, who taught me everything I know about cell culture. It's equally hard imagine that the time spent in the Ethier lab would have been half as enjoyable without my labmates. I owe a lot of laughs and good thoughts to discussions with Dr. Ian Campbell, Dr. Baptiste Coudrillier, Dr. Julia Raykin, Dr. Robert Rankin, Dr. Andrew Feola, Eric Snider, Ke Wang, Stephen Schwaner, Jhon Magdaleno, and Michael Jennings.

I am also deeply indebted to Brian and Viki Norman, and John and Marcia Dabkowski, who have been there with encouraging words, home cooked meals, and unwavering support for me every step of the way.

TABLE OF CONTENTS

LIST OF TABLES

LIST OF FIGURES

LIST OF ABBREVIATIONS

AFM	Atomic Force Microscopy
ALD	Axonal Loading Device
APDL	ANSYS Parametric Design Language
B	Left Cauchy-Green deformation Tensor
DM	Differentiation Medium
ECM	Extracellular Matrix
FEM	Finite Element Model
GM	Growth Medium
I	Invariants of the left Cauchy-Green Deformation Tensor
IOP	Intraocular Pressure
J	Volume ratio
LC	Lamina Cribrosa
ONH	Optic Nerve Head
PBS	Phosphate Buffered Solution
PDMS	Polydimethylsiloxane
RA	Retinoic Acid
RGC	Retinal Ganglion Cell
SA	Specific Aim
TBI	Traumatic Brain Injury
W	Strain Energy Function
σ	Cauchy Stress

SUMMARY

Glaucoma, the second leading cause of blindness world-wide, affects c. 2.8 million people in the US, of which 130,000 are legally blind. Vision loss during glaucoma is due to damage to, and the eventual death of, retinal ganglion cells (RGCs), neurons that carry visual information from the eye to the brain. One current theory hypothesizes that the mechanism of RGC death during glaucoma is due to changes to the local mechanical environment of the RGCs, specifically the existence of additional stresses and strains acting on the axons of the RGCs, resulting in their dysfunction. As this environment is difficult to access in vivo, little is known about the pathway from mechanical insult to RGC dysfunction.

This work presents an *in vitro* platform for studying the effects of physiologically relevant, axonally applied mechanical insult to neurons in culture. Design considerations are presented, and finite element studies are shown to establish proof of concept. The mold for creating the device was microfabricated in a cleanroom for use in the replica molding of the device. The process of fabricating the final device is then detailed. Initial biocompatibility assays are presented, and experiments for characterizing the function of the device are proposed.

Suggestions for future uses of the device include basic science research to elucidate the cellular response of neurons, specifically RGCs in the context of glaucoma, to mechanical insult. Furthermore, the device could be used in preliminary testing of the efficacy of neuro-protective agents before progression into animal models.

Chapter 1 Introduction

1.1 Glaucoma

Glaucoma is a collection of optic neuropathies affecting the visual pathway, and is the second leading cause of blindness world-wide. There were an estimated 60 million individuals affected by the disease in 2010, a number which is projected to increase to over 79 million by 2020 [1, 2]. Approximately 2.8 million people in the US suffering from glaucoma, of which 130,000 are legally blind [1]. According to Rein *et al.*, Glaucoma results in upwards of $2.9 billion annually in direct medical costs, with billions more in indirect costs due to reductions in productivity, lost tax revenue, and Social Security payouts [3].

The characteristic symptom of glaucoma is patterned visual field loss, which begins at the periphery of the visual field, and progresses inwards with time. Glaucomatous vision loss is due to the dysfunction and eventual death of the retinal ganglion cells (RGCs), the neural cell type which carries visual information from the retina to the visual cortex in the brain [4]. Due to a lack of other detectable symptoms of the disease, glaucoma is typically not diagnosed until 30% to 50% of retinal ganglion cell axons have been lost, resulting in significant changes to the visual field, as shown in Figure 1 [5]. This functional outcome is typically accompanied by morphological changes to the optic nerve and optic disc due to the loss of the RGCs, as well as active remodeling of the tissue due by astrocytes (See Figure 1) [6].

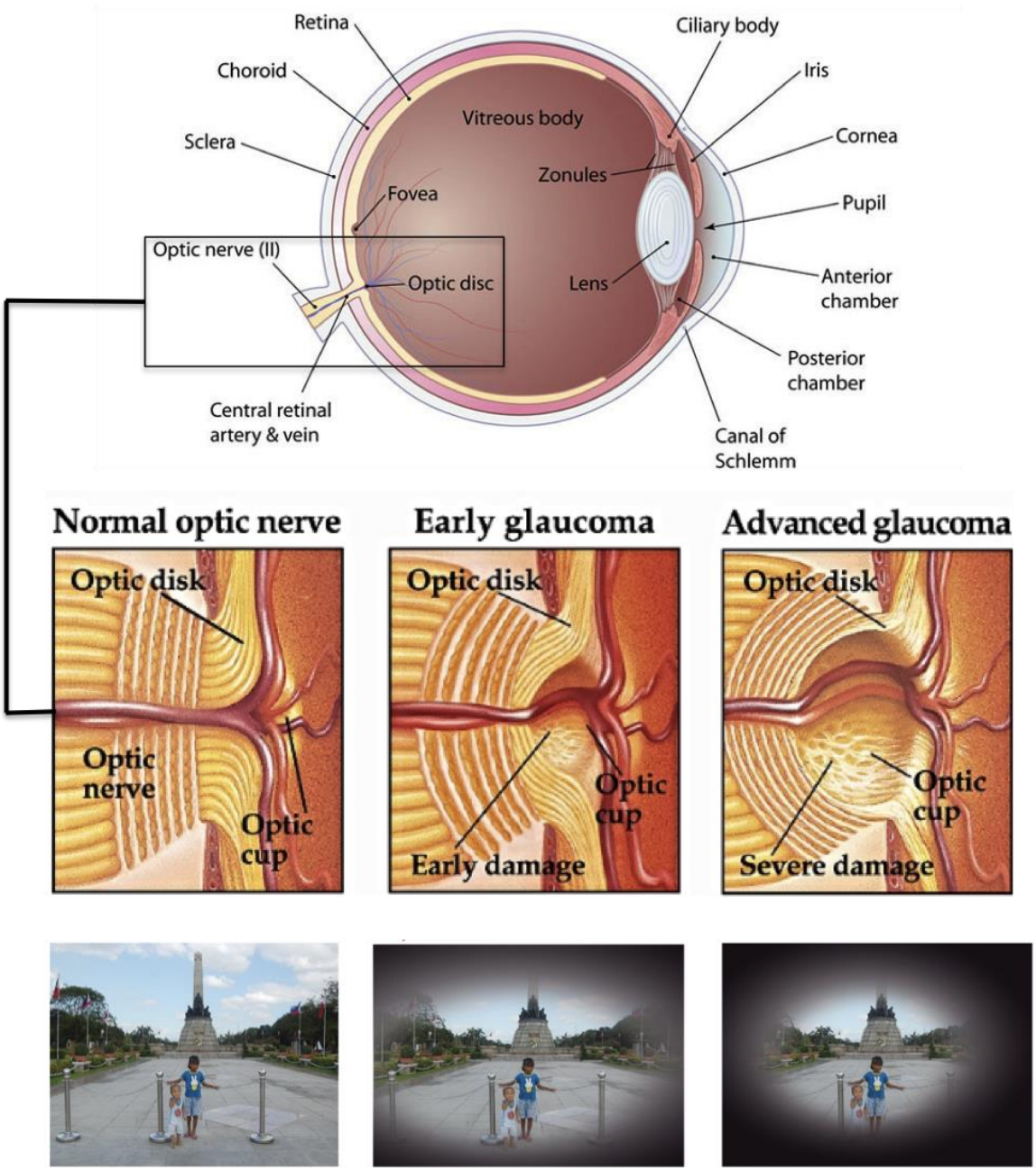

Figure 1: Top: Diagram showing the anatomy of the eye. From [7] Middle: Schematic diagram showing the morphological changes to the optic disc during the progression of glaucoma. From [8] Bottom: Image depicting the progression of the patterned visual field loss due to glaucoma. From [9]

According to clinical studies, increased intraocular pressure (IOP) has been identified as the largest risk factor for glaucomatous damage [10]. Additionally, treatments which reduce the IOP have been shown to be effective in slowing, or even preventing, the progression of glaucomatous vision loss in patients with both physiological (21 mm Hg or lower) and pathological (greater than 21 mm Hg) levels of IOP [11]. Thus, elevated IOP is a so-called "causative risk factor" [12]. Other risk factors for developing glaucoma include age, myopia, a family history of glaucoma, African ancestry, and certain morphological features of the optic disc [12, 13].

One of the current theories for how the increase in IOP leads to vision loss is the so-called "mechanical hypothesis" of glaucoma [14]. This hypothesis suggests that the structural components of the eye are under considerable levels of mechanical stress due to the IOP, and that the increased IOP further distorts the tissue of the optic nerve head (OHN), resulting in mechanical insult to the RGC, which may then lead to their dysfunction, and eventual death. This theory will be presented in greater depth in the Background section.

As the environment of the ONH, where the axons are thought to experience the mechanical insult, is physiologically complex, and difficult to access *in vivo*, the direct effects of increased IOP on the RGC axons are difficult to assess. This project was embarked upon in order to create a platform to subject RGC axons to graded mechanical insult in a very controlled and accessible environment.

1.2 Specific Aims

The overarching goal of this project is to design, manufacture and characterize an axonal loading device (ALD). In order to assess the success of this project, four specific aims (SA) were established.

Specific Aim 1: To establish a feasible design of a device capable of *in vitro* axonal compression experiments, simulating the mechanical insult that retinal ganglion cell axons have been theorized to experience during glaucoma. This aim includes selection of the materials to be used, and finite element modeling of the device to establish proof of concept.

Specific Aim 2: To establish a reproducible process flow for the manufacture of the silicon wafer and SU-8 based master mold for the device of SA1. The design resulting from the first specific aim required a complex micro-manufacturing process to reliably create the mold features, which are on the order of tens of microns. While baseline manufacturing parameters for the micro-manufacturing of the mold can be gleaned from the literature, the general instructions for a given fabrication step frequently do not yield the expected results, driving the need for the parameters of the micro-fabrication process to be empirically determined to achieve the desired results.

Specific Aim 3: To verify the biocompatibility of the device by maintaining cells in culture on the device, similar to the situation that would occur during long term experiments. It has been shown that neurons in culture require days to extend their axons the hundreds of microns needed to separate the axons from the cell bodies.

Specific Aim 4: To characterize the axonal injury function of the device. Outcomes of the cellular biomechanics experiments with the device will rely upon the correlation of axonal deformation to pathophysiological effects.

Chapter 2 Background

2.1 Ocular Anatomy and Physiology

To better understand the basics of the mechanics of glaucoma, and the motivation behind the development of an axonal loading device, a brief overview of the most relevant aspects of ocular anatomy will be presented.

2.1.1 Intraocular Pressure

Intraocular pressure (IOP) is the fluid pressure within the eye and is determined by the flow of aqueous humor into and out of the anterior chamber, the region between the cornea and lens (see Figure 2). In many forms of glaucoma, it is thought that defects in the system which regulates the IOP are the cause of the glaucomatous damage [15]. Indeed, lowering the IOP in patients suffering from glaucoma is currently the standard treatment for the disease [11]. Physiological levels of IOP range between 10 to 21 mm Hg, while patients with IOP levels greater than 21 mm Hg are considered to be at higher risk for developing glaucoma [10].

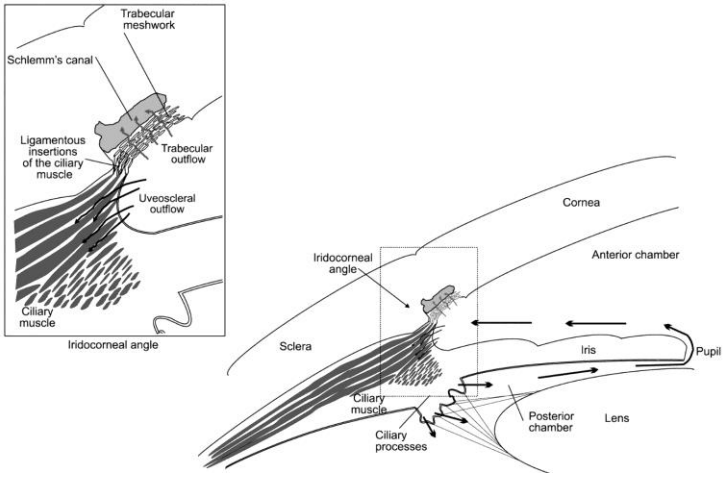

Figure 2: A schematic showing the secretion of aqueous humor from the ciliary processes, its flow from the posterior to anterior chambers, followed by the outflow through the trabecular meshwork and uveoloscleral pathways. From [16]

2.1.2 The Sclera

The sclera, the main structural component of the eye, is a soft tissue comprised mainly of layers of collagen fibers (>50%), and acts in part to contain the forces due to the IOP in order to create a rigid and resilient globe [17]. The mechanical properties of the sclera enable it to withstand forces inflicted by external trauma, as well as to maintain the shape of the globe during transient IOP fluctuations due to blinking, eye rubbing, the ocular pulse, and diurnal changes in the IOP. The microarchitecture of the sclera, in both the thickness of the layers of collagen, and the arrangement of the collagen fibers varies locally, as shown in Figure 3 [17, 18].

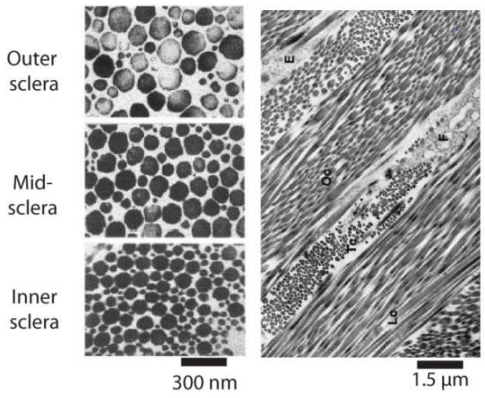

Figure 3: (A) Transmission electron micrograph showing variation in collagen properties in the outer, mid, and inner sclera of a tree shrew. Adapted from [19]. B) Electron micrograph image of the human sclera showing organized layers of collagen fibers. Adapted from [20].

2.1.3 The Optic Nerve

The optic nerve is formed where the RGC axons from throughout the retina's nerve fiber layer converge to exit the eye, as illustrated in Figure 4. After the axons exit the globe, the RGCs do not synapse until they reach the brain, a distance which can be upwards of 5 cm [21]. After

reaching the brain, the axons project to the lateral geniculate nucleus, pretectal nucleus, and suprachiasmatic nucleus, providing visual information to create images, cause reflexive eye movements and to help establish the circadian rhythm, respectively [22].

As the RGC is not capable of synthesizing function-critical enzymes and proteins in its axon, it must transport these factors along the length of the axon, i.e. from the eye to the brain [23]. This process, known as axoplasmic transport, is known to be one of the cellular processes which is disrupted during glaucoma. Further, studies have linked this disruption of axonal transport to neuronal dysfunction and death [23] [24].

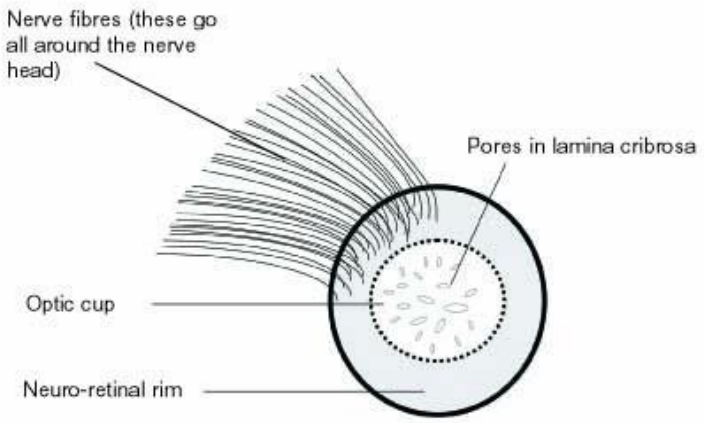

Figure 4: Cartoon of part of the nerve fiber layer coming together to form the optic nerve. Adapted from [25]

The axons of the optic nerve remain unmyelinated until they pass through the lamina cribrosa, where they are myelinated by oligodendrocytes in the post-laminar space, and as such are particularly vulnerable to insult as they pass through the lamina. Mean axon counts of the optic nerve report 1,158,000 fibers per nerve (range; 777,000 – 1,679,000), a number that has been

shown to decrease significantly with age [26]. Further, this loss is greatly accelerated during the progression of glaucoma [27], and is directly associated with the severity of vision loss.

2.1.4 Optic Nerve Head

The optic nerve head (ONH), shown in Figure 5B, is comprised of the RGC axons as they come together to form the optic nerve, and of the structural tissues important in maintaining the mechanical integrity of the scleral canal, which is the gap in the scleral shell where the optic nerve exits the globe. The lamina cribrosa (LC, seen in Figure 5C) is the main structure which partially fills and gives structural support to the scleral canal with a latticework of collagen. The collagenous pores found in the LC range from 25 μm to 250 μm in diameter, with variations in pore size found throughout the entire LC. Additionally, astrocytes have been found to cover the collagenous beams of the LC. These astrocytes serve to produce the extracellular matrix (ECM) found in the LC, consisting of type I, III, and VI collagen and elastin [12]. Furthermore, the astrocyte processes form a second, finer meshwork within the fibrous collagen network of the LC. These processes divide the larger pores into sub-pores that range from 2.5 μm to 5 μm in diameter, which act to separate large groups of axons into smaller bundles [28]. The beams of connective tissue that make up the latticework of the lamina cribrosa contain capillaries that supply nutrients and oxygen to the axon bundles that are passing through the pores.

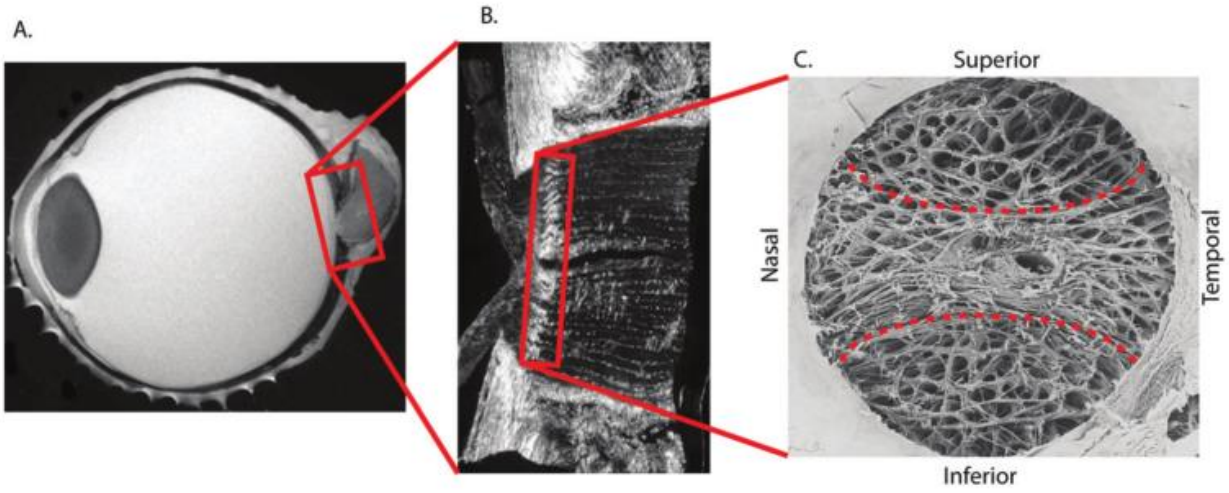

Figure 5: (A) Anatomy of the eye, showing the location of the (B) optic nerve head, which contains the (C) lamina cribrosa (en face view from B). Figure from [12].

2.2 Axonal Injury during Glaucoma

One theory for how the increase in IOP leads to RGC damage at the LC is the so-called "biomechanical hypothesis" of glaucomatous damage. According to this theory, the sclera, ONH, and other ocular tissue are constantly under IOP-induced stress and strain at physiological IOP levels [14]. However, during glaucoma, the change in IOP leads to increased levels of stress and strain, due to additional deformations to the scleral shell. The alignment and thickness of the collagen fibers found in the peripapillary sclera, the portion of the sclera surrounding the LC, results in a very stiff tissue when compared to the stiffness of the ONH. This difference in mechanical properties causes the ONH to be particularly susceptible to the biomechanical effects of elevated IOP [29]. For example, the stress imposed by increased IOP may cause changes to the microstructure of the LC, distorting both the connective tissue and astrocyte networks, as shown in Figure 6.

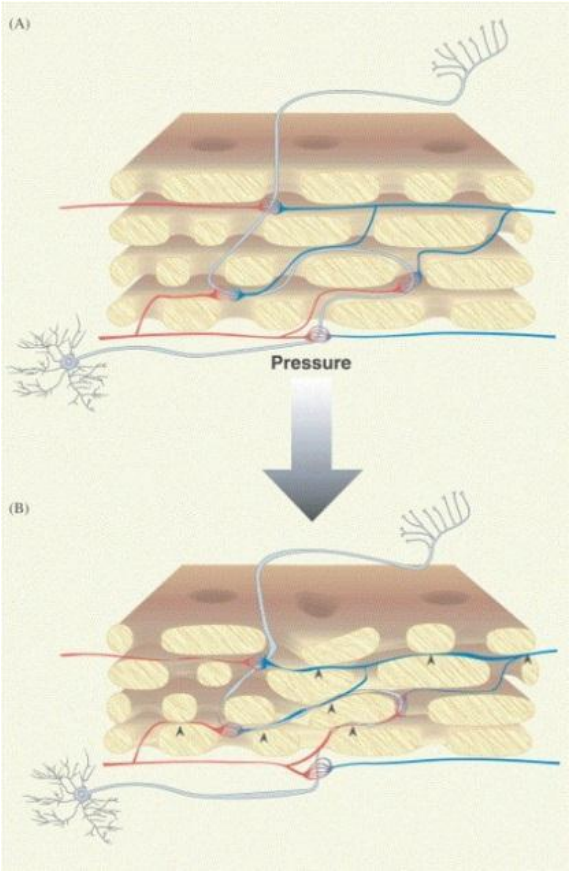

Figure 6: Posited changes to the pore network of the LC during increased IOP. (Upper) The LC, with RGC axons (grey), veins (blue) and arteries (red) passing through the pore network. (Lower) The same network after the increase in IOP. Black arrowheads indicate points where the pore network has collapsed, compressing the nerve and vascular tissue. Image from [30].

As previously discussed, the RGC axons must pass through the LC in order to exit the eye en route to the brain. Moreover, it has been shown that damage to RGCs during glaucoma may be initiated at the level of the LC. Thus, it is thought that the mechanical changes which are imparted by the sclera to the LC result in RGC dysfunction, including disruption of axoplasmic transport.

2.3 Models to Study Optic Nerve & RGC Biomechanics

Currently, there are many models which are used to study the effects of mechanical insult on the optic nerve, RGCs, and other neuronal cell types. These models, both *in vivo* and *in vitro*, have various advantages and disadvantages as systems for studying the response of neuronal tissue to various forms of insult.

2.3.1 In Vivo Models

There are several *in vivo* models of optic nerve insult, each of which has certain qualities which make it suitable for studying different aspects of damage to the visual system. In general, the advantage to using i*n vivo* models of glaucomatous insult is that they are able to provide insight into the organism-level response to the injury. However, it is also this aspect of *in vivo* models which makes the results from these models so difficult to analyze; the observed response to the investigated phenomenon may be the resulting combination of many converging, intertwining, and counter-acting responses.

One commonly employed method of studying the effects of mechanical damage to a large population of RGCs is the optic nerve crush model. In order to access the optic nerve, an incision is made in the conjunctiva, beginning at the inferior region, and continuing temporally around the globe. Micro-forceps are then used to grasp the edge of the conjunctiva, pull it back, rotating the eyeball nasally, and exposing the posterior pole of the eye and optic nerve. Researchers use care not to apply the injury to the blood vessels alongside the nerve. Typically, the crush injury will then be applied with cross-action forceps, at a location from 1-3 mm posterior to the globe, as shown in Figure 7. The duration of the crush can last anywhere from 1 to 10 seconds, at which point the optic nerve is released, and the globe is allowed to rotate back into place [31].

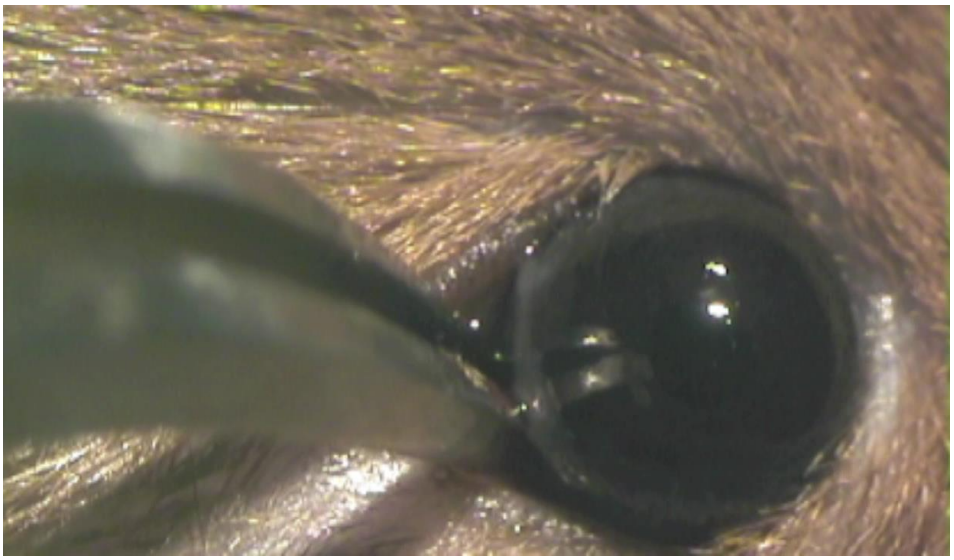

Figure 7: Image showing the technique of optic nerve crush in a mouse model. Image from [31]

This technique has been used to investigate the effects of optic nerve injury on axonal transport. This is achieved through the injection of a fluorescent tracker into the brain that is transported

anterograde along the RGC axon into the retina, allowing for an analysis of the changes in axonal transport due to nerve crush. An advantage to the model is that it allows for the global effects of an insult to an entire population of RGCs to be studied. Additionally, as the nerve-crushed organism is typically otherwise viable, long-term studies of RGC and retinal response can be evaluated.

Although this model of nerve injury applies a "focal" insult when viewed from the organism or organ level, the width of the forceps used to apply the insult is several orders of magnitude wider than the diameter of a single axon (~1-3 μm), and as such, results in a non-focal cellular injury. Moreover, it is difficult to assess the stress and strain applied to the axon, as the force of the crush is distributed across many axonal fibers as well as the surrounding connective tissue and glial cells. Also of note is that the axons have become myelinated at this point in the optic nerve, whereas they are unmyelinated as they pass though the LC. Further, the resulting effects of the optic nerve crush surgery to the RGC cannot be seen as simply the result of the mechanical insult, but must take into account secondary global responses such as inflammation. Additionally, it is very difficult to rigorously assess the damage that is caused by the crush through the life of a single animal, as the animal must be sacrificed, and tissues excised, in order to assess any cellular effects of the insult.

Furthermore, there are *in vivo* models of induced ocular hypertension which elicit glaucoma-like pathologies. Methods of inducing ocular hypertension include episcleral injection of hypertonic saline [32], episcleral vein cauterization [33], and laser photocoagulation of the trabecular meshwork [34]. The increase in IOP due to these techniques has been shown to be long-lasting (> 1 week), and can be somewhat controlled by the investigator in most cases [35]. The resulting RGC degeneration follows a pattern similar to what is seen during glaucomatous optic nerve

damage, making the model well suited for investigations into the long-term effects of ocular hypertension. While these models provides a good approximation of the pathogenesis of glaucoma, the nature of RGC insult and pathways through which RGC degeneration occur remain unclear.

In addition to conventional methods of inducing optic nerve damage, mice have been identified which exhibit spontaneously occurring, age-related increases in IOP [36]. The strain, referred to as the DBA/2J strain, has been shown to develop a pathology similar to that of glaucoma as it ages. Namely, chronic IOP elevation, the death of RGCs, optic nerve atrophy, cupping of the ONH, and defects in visual function are typically observed after nine months [37]. Disadvantages of this mouse for studying the effects of glaucomatous damage on RGCs are in line with all other *in vivo* models: a lack of access to the tissues of interest, and no way to discern the nature of the insult to the RGCs. Furthermore, this mouse has been shown to exhibit other ocular development issues, including pigment dispersion and iris atrophy. These issues with other ocular structures create an even more complex system for analyzing the effects of increased IOP on RGC dysfunction [37].

2.3.2 in Vitro Models of Neuronal Mechanical Insult

In vitro models of insult to neurons have also been introduced in the field as tools to study neuronal response to injury in the context of glaucoma [38], traumatic brain injury (TBI) [39], and other pathologies involving neuronal injury [40]. As with the *in vivo* models, *in vitro* models of RGC damage can be either direct, as with the optic nerve crush model, or indirect, sharing similarities with the induced ocular hypertension model. The general advantage to *in vitro* methods of experimentation is that the system in question is restricted to the cell type(s) or tissues being investigated, reducing the number of variables which may be affected by the

experimental protocol. Furthermore, the cells can be relatively easily accessed for applying the insult, as well as imaging pre-, during, and post-injury application, allowing the injury response to be observed with high spatial and temporal resolution.

One established method of inducing mechanical damage to neurons *in vitro* is to culture the cells on deformable substrates [41, 42, 43]. An example of such a device, seen in Figure 8, consists of two culture wells in which neurons are seeded, and an array of deformable polydimethylsiloxane (PDMS) microchannels which connect the two wells [44]. The microchannel array provides a method for isolating the axons from the cell bodies, as well as a way for the axons to traverse from one culture well to the other, forming functional synaptic connections. It is in the microchannel area that the stretch insult is applied by inflating a pressure chamber below the microchannels. Once inflated, the PDMS substrate is deformed upward, effectively increasing the distance that the axon is traveling, introducing strain. As the axons have attached to the PDMS substrate, the axons are stretched along with the substrate. Further, the design can be used to investigate the response of either single axons or axon bundles through the modification of the microchannel height and width.

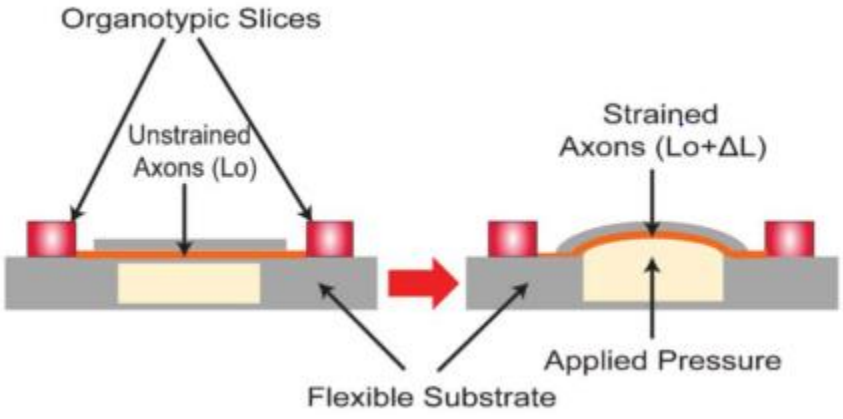

Figure 8: Uniaxial axonal strain device schematic before and after strain application. Image from [44].

This design is powerful for studying the effects of mechanical strain on neurons for several reasons. First, as the PDMS is optically clear, it allows for the visualization of axonal transport pre-, during, and post-strain injury. Secondly, the degree and rate of strain can be controlled through the inflation of the air chamber below the microchannel array. Also, as there are many microchannels connecting the two cell culture areas, large-scale experimentation on axonal injury can be relatively rapidly completed. While this model of axonal damage may be a powerful tool for the study of mechanical strain along the axis of the axon, the method of injury does not attempt to replicate the mode of injury hypothesized to occur in the "biomechanical hypothesis" of glaucomatous damage.

Another model of axonal injury which has recently been developed creatively uses the technique of atomic force microscopy (AFM) [45]. AFM is generally used as a technique for gathering information which can be derived from micro- to nano-meter scale deflections of a cantilever sensor as it is applied across a sample of interest. Common applications for AFM include determining mechanical properties of cells and tissues, creating 3-dimensional images of structures with micro- and nano-scale features, as well as measuring forces on the atomic scale.

In the axonal injury application using AFM, a 20 μm polystyrene bead is attached to the cantilever tip of the AFM, and is used to apply a pre-determined pressure, ranging from 0 to 1.6kPa, directly to the neuron. An array of PDMS microchannels reversibly-bonded to the cell culture substrate is employed to separate the axonal projections from the cell bodies prior to loading. Once the axons have migrated down the channels to sufficient lengths, the PDMS microchannel array is removed, exposing the axon to the environment, and allowing them to be accessed by the AFM tip, as seen in Figure 9.

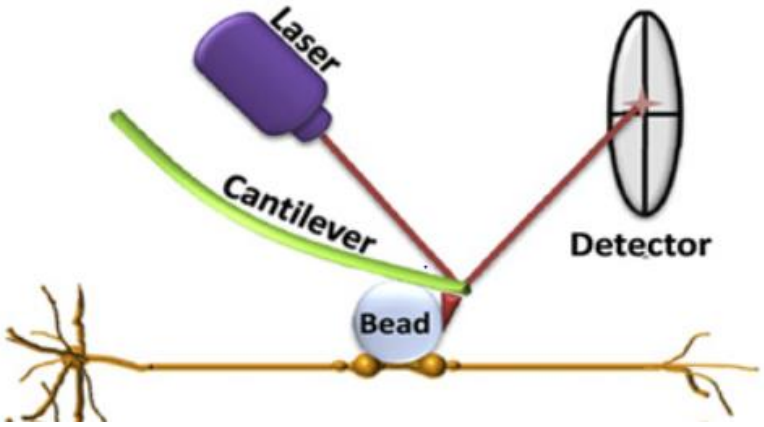

Figure 9: Schematic showing the application of AFM to axonal injury experiments. Image from [45]

This method of focal axonal insult would allow for very precise application of force in both magnitude and location along the axon, and is a very promising model of focal axonal insult. Additionally, this method could be employed to gain insight into the mechanical properties of the axons. The main disadvantage of this implementation is that each experiment would be gathering data from the loading of a single axon, making acquiring large amounts of data difficult and time consuming.

2.3.3 Astrocyte Response to Mechanical Insult

An additional cell type which has been shown to undergo significant changes during glaucomatous insult is the astrocyte population of the ONH. It has been shown that ONH astrocytes become activated during glaucoma, and that their activation leads to remodeling of the ECM of the ONH [6]. It is thought that this remodeling, triggered by the biomechanical changes in the eye that occur during ocular hypertension, may be responsible for altering the environment which the RGC axons must pass through, and ultimately, for the degeneration of the RGC. Other work [46] has shown that the reactive remodeling of the astrocytes can be reversed, if the

activating insult is removed early in the process. This demonstrates that the astrocyte response is nuanced, and is a function of not only the degree of ocular hypertension, but the time course that the pressure increase follows.

Despite evidence of maladaptive astrocyte behavior, they may also exhibit beneficial responses to certain modes of mechanical insult. For example, results pointing toward protective effects of activated glial cells in the optic nerve have been found in both *in vivo* optic nerve crush experiments, as well as *in vitro* populations of disassociated RGCs [47]. It was found that animals which received an optic nerve crush, while simultaneously inducing ocular hypertension to activate the astrocytes, saw an enhanced protective and even regenerative response in the RGCs. Additionally, it was observed that RGCs in co-culture with astrocytes increase the growth potential of the axons, as well as the neurite outgrowth of the culture, suggesting both a protective and regenerative role for astrocytes.

These studies suggest a complex role for astrocytes in the eye, with situation-dependent protective or maladaptive response to damage to the optic nerve. Further experimentation in both *in vivo* models to discern the global response, as well as *in vitro* work to better ascertain the direct relationship between RGC and astrocyte function, must be completed in order to better understand the role that astrocytes play in glaucoma.

2.4 Motivation and Previous Ethier-lab Work

Prior to this effort, there had been work done in the Ethier lab to address the need for an *in vitro* platform which would combine the advantages of damaging many axons at once, as in the axonal strain device, as well as the focal application of insult, as in the AFM compression model. This work, undertaken by Audrey Fahrny while at the Bioengineering Department at Imperial College

London, explored the possibility of creating two versions of an axonal loading device capable of applying graded mechanical insult to cells. While both designs were shown to be theoretically sound, time and manufacturing constraints did not allow for the fabrication of either device. These designs inspired some aspects of the device presented in this document, but operated on different principles. These designs will be reviewed here.

2.4.1 Microchannel Crush Design

The first design, seen in Figure 10, was a PDMS device based on an array of 101 compressible microchannels. The cell culture substrate and microchannels of the device were designed to be a monolithic PDMS slab, which was to be produced via soft-lithography from a patterned silicon wafer mold. A so-called Campenot chamber, a glass cylinder bonded to the PDMS substrate through the use of biocompatible silicon grease, was to be used to separate the axons from the body of the RGC. The interface of the PDMS substrate with the silicon grease forms a semi-permeable barrier. This barrier allows the growth of axons into the microchannel array area, but prohibits the entry of the larger somas of the neuron [48]. Once past the silicon grease barrier, the axons would be able to freely migrate into the microchannel area, and into one of microchannels for axonal crush experiments.

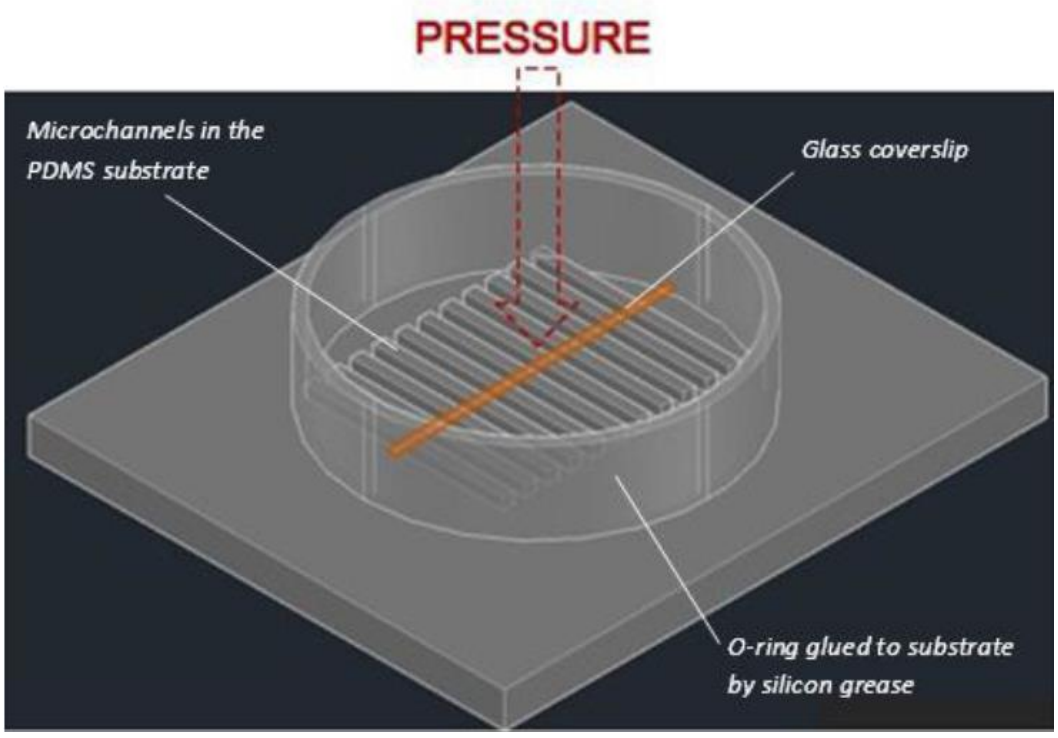

Figure 10: The PDMS-based microchannel device. Image from [30].

After axons migrated into the microchannels, a custom load-bearing glass coverslip (width: 400 µm) would be placed atop the microchannels, spanning the entire array of channels. In order to apply load to the axons, the coverslip would be loaded with weights, deforming the PDMS microchannels. Once the channels had deformed to the height of the axon, the coverslip would contact the neuron, stressing the axon. Additional weights would then be added to compress the neuron to varying degrees.

The large number of microchannels included in the design would allow for the large-scale crushing of axons and collection of data. Another advantage to this model of injury was that the optically clear PDMS material would allow for *in situ* imaging. Both of these features were considered in the design of the device presented in this thesis.

However, the proposed method of loading the cells left room for variation between experiments, due to possible variations in the placement and measurement of the weights used to load the coverslip. Additionally, the width of the crushing coverslip, 400 μm, would crush a length of axon approximately as long as the entire thickness of the LC, questioning the focal nature of the insult [49]. This design was not manufactured due to problems with the fabrication of the master mold.

2.4.2 Porous Membrane Model

The second design, seen in Figure 11, a porous membrane model of axonal damage, was an attempt to create a more biofidelic model of axonal injury. The design consisted of a modified Transwell® 3-D cell culture assembly, with an additional porous PDMS membrane mounted to the underside of the chamber. The neurons would be seeded into the Transwell® system, and cultured according to established protocol. After the neurons had attached and began extending axons, it was hypothesized that the axons would migrate through the pores in the Transwell®, while the cell bodies would be restricted to the upper area by the size of the pores of the membrane (pore diameter: <3 μm). The additional porous PDMS, mounted directly below the Transwell® membrane, would allow for the axons to pass through the PDMS array of pores, such that the axons would pass through both the Transwell® and PDMS membranes.

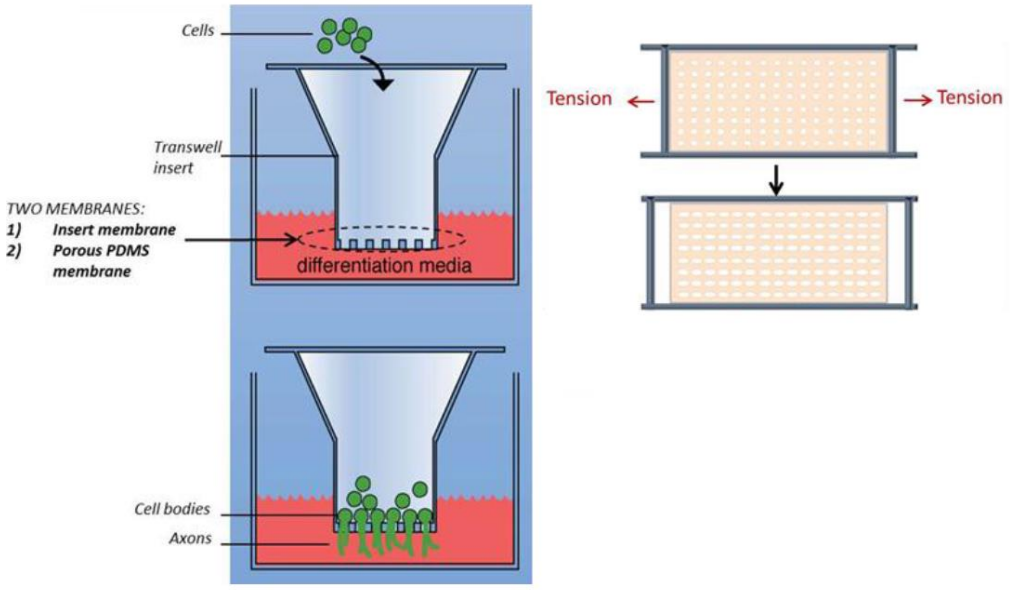

Figure 11: The biofidelic model, showing the Transwell ® culture system, on the left, and the proposed deformation of the porous PDMS membrane on the right. Image from [30]

Once the axons had extended down into the PDMS pore array, this membrane would be subjected to uni-axial tension, which would deform the pores of the PDMS membrane. The deformation of the pores would then impart stresses and strains to the axons that were growing through the pores.

The main advantage to this design was that it was thought that this method of axonal damage would more closely replicate the maladaptive changes which occur in the LC during glaucomatous injury. However, this model of axonal injury was not suited to *in situ* imaging of axonal transport, as the axons would not be easily accessible. Additionally, initial manufacturing tests showed that the porous PDMS membrane was prohibitively difficult to manufacture and handle. A prototype device was never completed

Chapter 3: Design and Analysis

3.1 Design and Considerations

As stated in the previous chapter, the response of retinal ganglion cells to mechanical insult has not been well characterized, and current methods are not well suited for the collection of large amounts of axonal loading data. Thus, this project was designed to fill this technological gap. In order to guide the development of a device, the following set of requirements for an axonal loading device (ALD) were determined.

1. Must be able to support long term cell culture in order to allow for axonal migration.
2. Must include a means to separate the cell body from axonal portions of the neuron.
3. Must allow a method to apply a graded, focal mechanical insult to the axonal portions of the neuron.
4. Must be compatible with optical assessment of axonal transport and degree of damage during the course of axonal crush experiments.
5. Must be capable of running several concurrent crush experiments to gather large data sets.

With these requirements in mind, a device with three functional areas was designed (Figure 12). A description of the considerations underlying the device design follows.

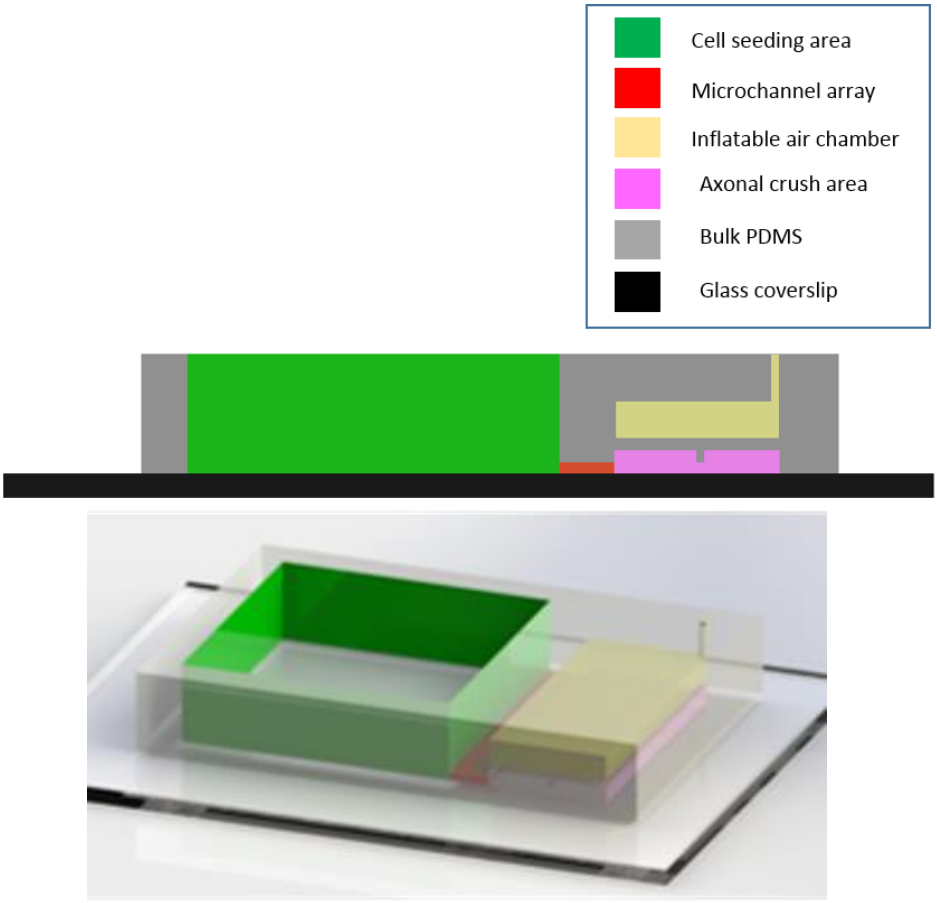

Figure 12: Upper: Cross sectional schematic of the ALD. Not to scale. Lower: Isometric view of a rendering of the ALD. Not to scale.

3.1.1 Cell Seeding Area

The cell seeding area, seen in green in Figure 12, was a 49 mm^2 area that was connected to the axonal crush area of the device through several arrays of microchannels. It was designed to be large enough to provide sufficient surface area to seed cells, and to be accessible via glass micropipette for single-cell electrophysiology readings [50]. This design was also consistent with several methods of delivering fresh cell culture medium to cells, including constant flow

perfusion systems, manually pipetting medium in and out, or by placing the entire device in a petri dish flooded with cell culture medium.

The height of the walls that define the cell seeding area was able to be changed as needed. For example, the wall height could be increased to accommodate a larger volume of medium in a device, or decreased to reduce the amount of medium required to flood a petri dish to provide the cells with medium. The device height is dependent upon the volume of PDMS that is poured into the mold. The standard height chosen for the cell seeding area wall height was 5 mm, which required approximately 30 mL of mixed PDMS elastomer. The set of standard dimensions allow for approximately 125 µl of medium per device.

Table 1: Dimensions of the cell seeding area

Length	7 mm
Width	7 mm
Height	5 mm* * dependent upon PDMS volume used in the molding process

3.1.2 Microchannel Array

Six parallel microchannel arrays, shown in red in Figure 12, were used in the design to separate the RGC axons from the cell bodies, and connect the cell seeding area to the axonal crush area. The height, length, and width of the individual microchannels in the array were chosen to allow only axons to traverse each channel [50, 51]. Previous work on axonal separation devices have

shown that microchannels less than 15 μm in width and height are sufficiently small to block the migration and expansion of cell bodies into and along the microchannels. Thus, the height and width of each microchannel were chosen to be 10 μm. Furthermore, the length of the microchannel was chosen so as to allow the passage of axons to the axonal crush compartment, while being long enough to block the migration of dendrites and other non-axonal projections [51]. In order to enable experiments which test if the proximity of the injury to the cell body had an effect on the cellular response, 3 different microchannel designs were incorporated into the mold. Two of the devices on the mold (Devices 1 and 4) had microchannel lengths of 250 μm, two more (Devices 2 and 5) had microchannels of length 300 μm, and a final pair (Devices 3 and 6) had channel lengths of 450 μm. Each device contained a set of six parallel microchannel arrays, leading to 6 separate axonal crushing compartments, extending from the cell seeding area, with each array having forty channels each. These 240 channels per device ensured that large data sets could be collected during each set of experiments.

Table 2: Microchannel dimensions

Microchannel Array Count	6
Microchannel Count per Array	40
Microchannel Height	10 µm
Microchannel Width	10 µm
Microchannel Spacing	15 µm
Microchannel Length (Devices 1, 4)	250 µm
Microchannel Length (Devices 2, 5)	300 µm
Microchannel Length (Devices 3, 6)	450 µm

3.1.3 Axonal Crush Area

The last area of the ALD, the axonal injury compartment, was the portion of the device where mechanical insult was applied to the axons. The axonal injury compartment consisted of a confined area which the axons could migrate into, shown in pink in Figure 12, and a pneumatically actuated deformable ceiling, shown in gold in Figure 12. It was based on the operating principle of the microfluidic valve developed by Unger and colleagues in 2000 [52]. In order to ensure that the insult was applied over a precise area, a downward projection from the ceiling was implemented in the design. This extension ran the length of the deformable ceiling, and was 30 µm in width. The master mold incorporated two different dimensions for the width of the deformable ceiling, 250 µm and 500 µm. These dimensions in turn dictated how far the axons had to migrate beyond the channels in order to be crushed by the projection, namely 125 µm and 250 µm respectively. These dimensions were chosen so that the displacement of the ceiling projection was not influenced by being too close to the structures supporting the ceiling, and assumes that the axons will continue to migrate for 125 µm or 250 µm in the direction established by the microchannels. This is an assumption which may not be valid for all axons and will need to be tested further. The height between the glass substrate and the crush pad portion of the PDMS membrane was chosen to be 10 µm, allowing the features of the crush pad to be defined using the same photolithography step as used in the microchannel array.

Table 3: Axonal injury compartment dimensions

Crush Area Width (Chips 1,3,5)	500 µm
Crush Area Width (Chips 2,4,6)	250 µm
Crush Area Length	1000 µm
Crush Area Height	10 µm
Crush Pad Width	30 µm
Crush Pad Height	30 µm

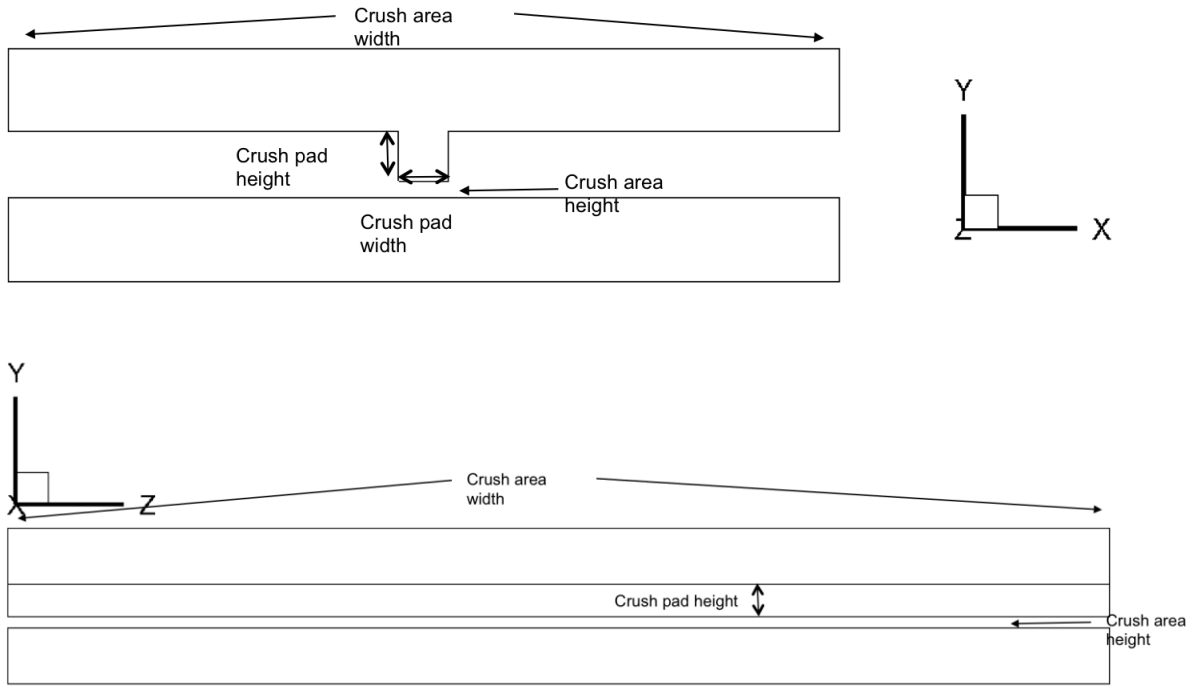

Figure 13: Cross sectional schematic of the axonal crush area of the ALD, showing (top) a section through the X-plane, and (bottom) a section through the Z-plane

3.2 Finite Element Modeling

In order to verify and refine the design of the axonal injury compartment of the device, several cycles of finite element modeling (FEM) were completed. FEM is a computational method used to solve differential equations and thus model the behavior of physical systems. Briefly, FEM subdivides a large, complex geometry into a set of subdomains, through a process known as meshing. The governing equations of the system are then solved in an approximate way on these subdomains.

3.1.1 FEM: Methods and Parameters

A structural finite element model of the axonal injury compartment portion of the ALD was created to verify that PDMS would be a viable material for the device, to show that the axonal crushing function of the device would operate as conceptualized, and to characterize the deformation of the crushing mechanism as a function of input pressure. FEM was used to model the response of a thin membrane of PDMS to a pressure which was uniformly applied to the upper surface of the membrane. The geometry of the PDMS structure and loading conditions were defined using the ANSYS Parametric Design Language (APDL). This method of defining the experimental parameters was chosen due to the ease of altering the geometry of the structure, material properties, and experimental conditions.

The software package used for the FEM was ANSYS 15.0 (ANSYS, Inc.). TecPlot 360 EX 2013, R1, TecPlot 360 EX 2014, R2 (Tecplot, Inc.) and MATLAB R2013b (The MathWorks, Inc.) were used for the post-modeling analysis. The geometry and material properties used to inform the finite element model are given in Table 4.

Table 4: Material properties and geometries of the finite element experiments

Elastic Modulus of PDMS	750,000 Pa [53]
Mass Density of PDMS	920 kg/m^3 [53]
Poisson Ratio of PDMS	.5 [54]
Elastic Modulus of Glass	72,000,000 Pa [55]
Mass Density of Glass	2510 kg/m^3 [55]
Poisson Ratio of Glass	.208 [55]
Width of Crush Ceiling and Glass	500 µm
Length of Crush Ceiling and Glass	1000 µm
Thickness of Crush Ceiling and Glass	50 µm
Distance between Ceiling and Glass	10 µm

The assumptions used in the creation of the model were as follows:

1. The resistance to deformation of the RGC axon is negligible compared to the PDMS and glass structures [56].
2. The glass substrate can be modeled as a linearly elastic material [57].
3. PDMS is an incompressible material [58].

4. The PDMS membrane can be modeled using the hyperelastic Mooney-Rivlin constitutive relationship [59].
5. The pressure in the deformation bladder is constant, and loads ceiling of the axonal crush area equally.

Zero displacement boundary conditions were imposed on the glass coverslip on the planes facing the negative Y, positive X and negative X directions (see Figure 14). Additional zero displacement conditions were imposed on the front, left, right, and rear-most faces of the PDMS membrane.

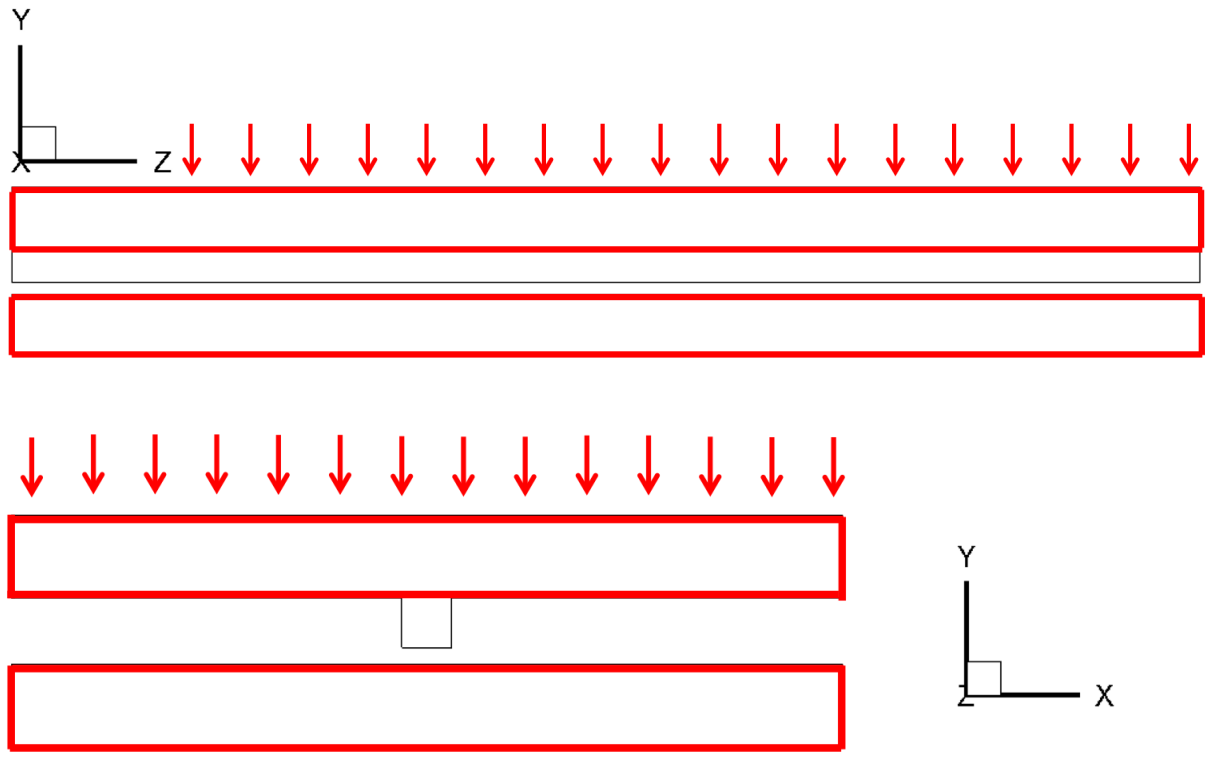

Figure 14: Experimental conditions of the FEM of the ALD. Red outlined planes indicate zero displacement boundary conditions. Red arrows show the input pressure which deforms the PDMS membrane downward.

3.1.1.1 The Mooney-Rivlin Constitutive Relationship

The Mooney-Rivlin constitutive relationship is used for describing the non-linear behavior of incompressible materials, such as elastomers and rubbers, and was chosen to model the behavior of PDMS in this FEM study. The Mooney-Rivlin model of hyperelasticity for an incompressible material such as PDMS can be described by the following stress-strain relationship

$$Eq\ 1:\ \sigma = 2J^{-1}[\ I_3 \frac{\partial W}{\partial I_1}\boldsymbol{I} + \left(\frac{\partial W}{\partial I_1} + \ I_1 \frac{\partial W}{\partial I_2}\right)\boldsymbol{B} - \frac{\partial W}{\partial I_2}\boldsymbol{B}^2$$

where σ is the Cauchy stress, J is the volume ratio, I_1, I_2, and $I_3$are the invariants of **B**, which is the left Cauchy-Green deformation tensor, and W is the strain-energy function. The strain energy function for an incompressible material in the Mooney-Rivlin model can be described by Equation 2:

$$Eq.2:\ W = C_1(I_1 - 3) + \ C_2(I_2 - 3)$$

where $C_1$and C_2 are material-specific constants.

3.1.2 Crush Pad Modeling

Initially, the axonal crush area relied on the deformation of the PDMS membrane alone to contact and deform the RGC axons. This design is seen in Figure 15. The PDMS membrane was modeled with 125,000 tetrahedral elements (SOLID185), while the glass substrate was modeled with 15625 tetrahedral elements (SOLID 185). This meshing density was chosen after a sensitivity study was completed which found the above meshing densities to be the most sparsely the geometry could be modeled, while still maintaining consistent deformation results. The meshing density was increased until the change in displacement due to the input pressure was within 1%. The upward facing (positive-Y facing) surface of the glass volume was defined as the

target surface (TYPE2 in ANSYS nomenclature) for the sake of contact modeling, while the lower (negative-Y facing) surface of the PDMS volume was designated as the contact surface (TYPE3).

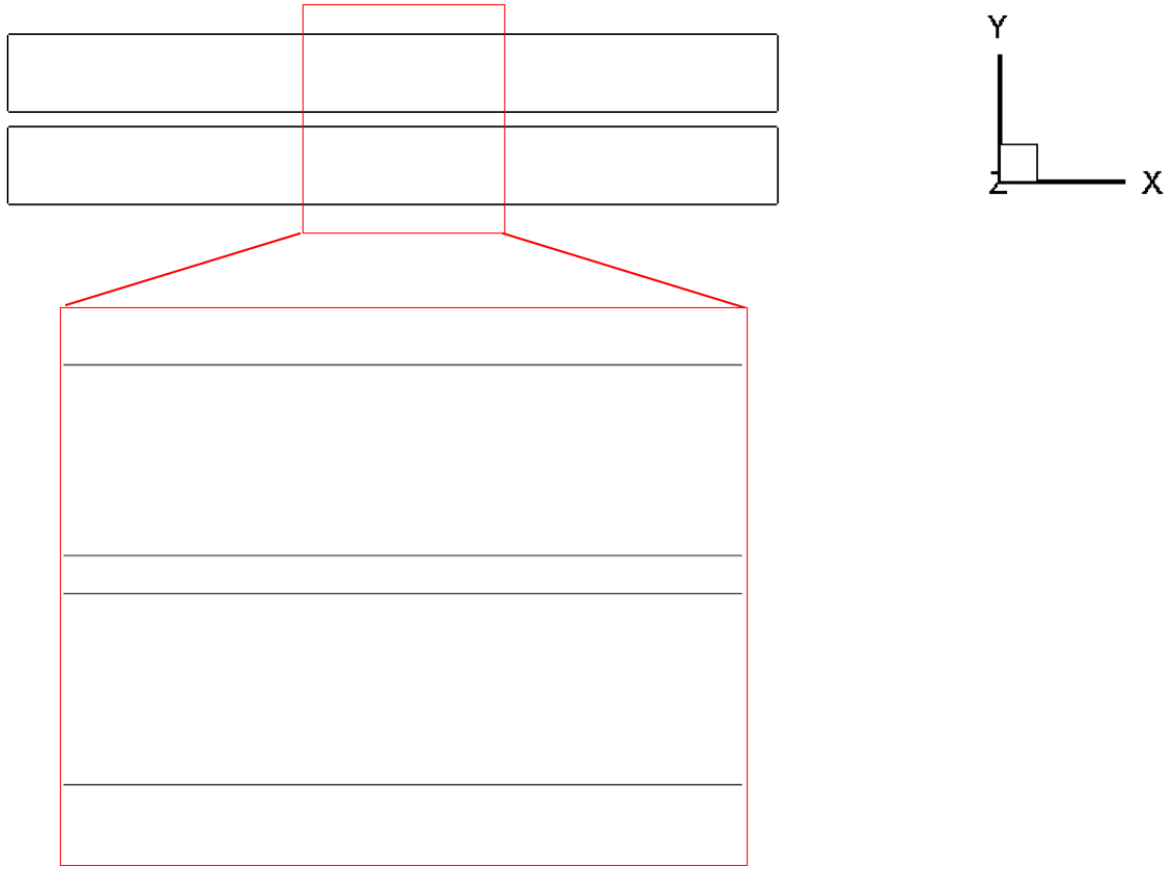

Figure 15: Schematic showing the initial axon crush area design. Inset shows the detail of the initial axon crush area design. The top area is the deformable PDMS membrane, while the lower is the glass substrate.

The FEM study of the original design showed that there was large variability in the contact area along both the Z and X axis of the membrane, dependent on the magnitude of loading on the membrane (Figure 16, Figure 17, and Figure 18). This change in area affects the area of the region where injury is applied. This design would thus have the issue that the area over which the

crushing pressure is applied would change as a function of the input pressure, and would increase as the input pressure was increased This variable contact area would then complicate studies investigating the effects of the magnitude of mechanical insult on the neurons, as the area over which the force is applied would change along with the magnitude of the insult.

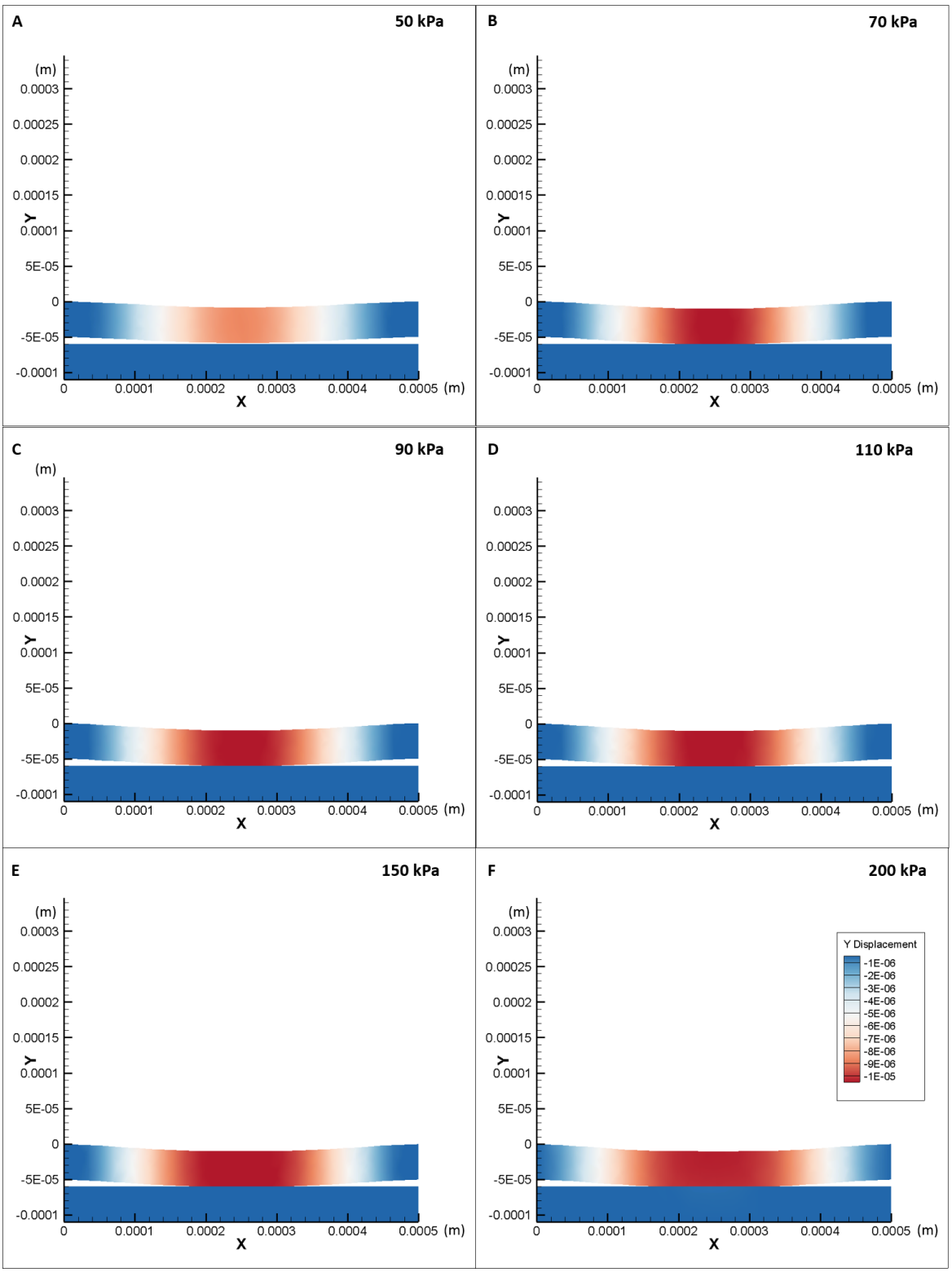

Figure 16: PDMS membrane Y-deformation vs. X location at loading pressures of A) 50kPa, B), 70kPa C), 90kPa D) 110kPa, E) 150kPa, F) 200kPa. The slices shown are taken from the middle of the Z-plane, at a plane furthest from the boundary conditions, in order to reduce edge effects.

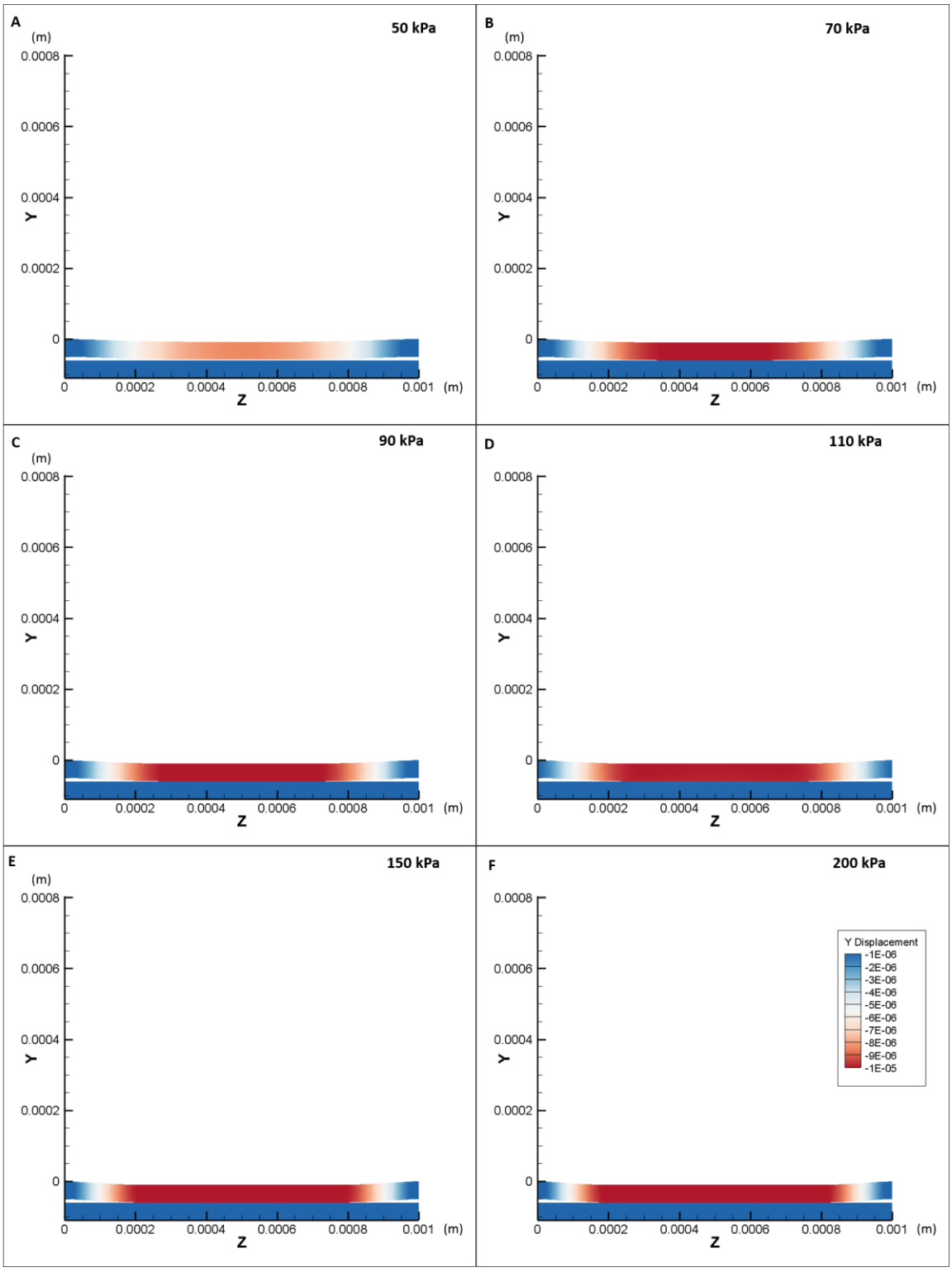

Figure 17: PDMS membrane Y-deformation vs. Z location at loading pressures of A) 50kPa, B), 70kPa C), 90kPa D) 110kPa, E) 150kPa, F) 200kPa. The slices shown are taken from the middle of the X-plane, at a plane furthest from the boundary conditions, in order to reduce edge effects.

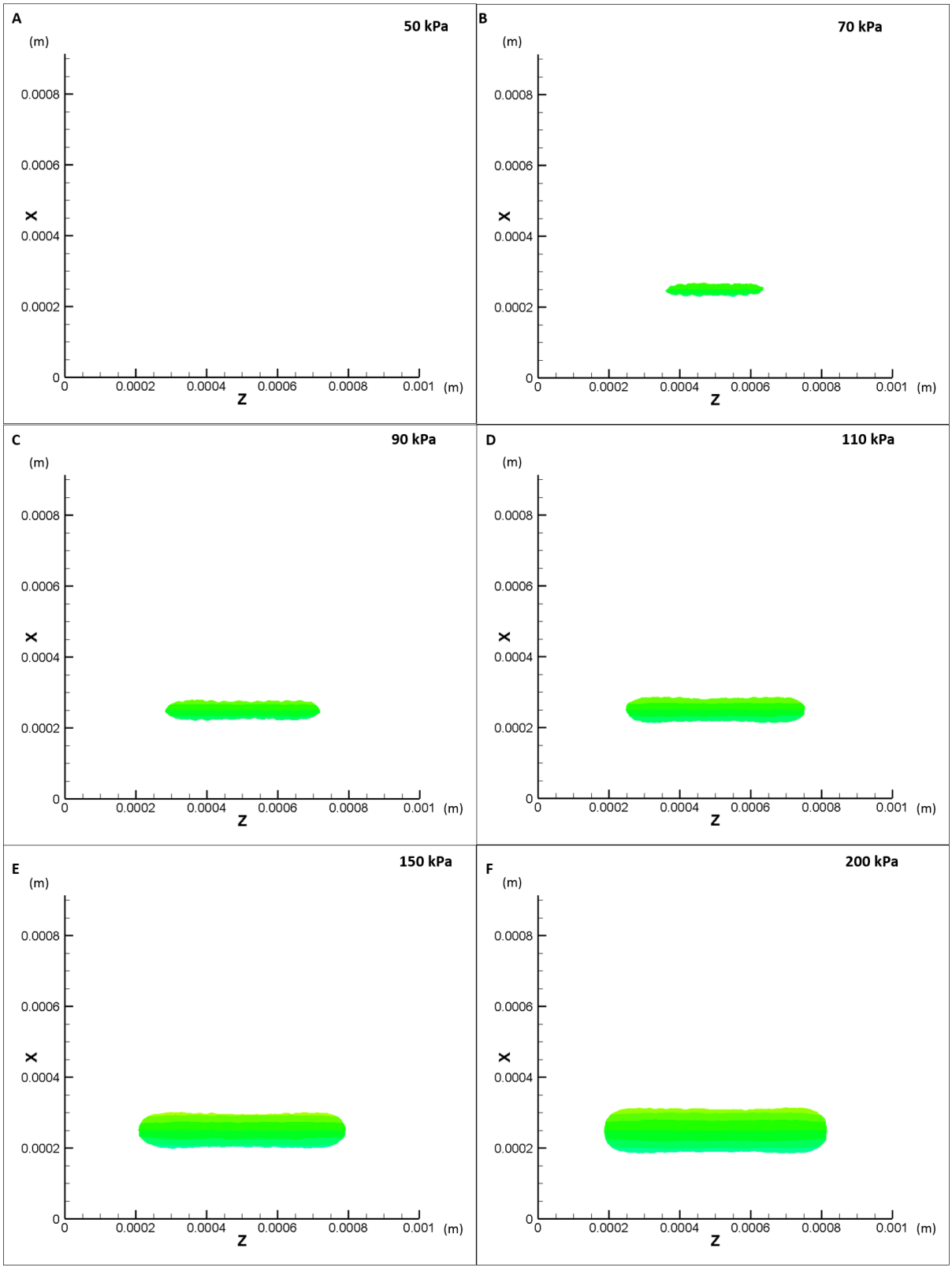

Figure 18: Contact area of PDMS with the glass substrate for loading pressures of: A) 50kPa, B), 70kPa C), 90kPa D) 110kPa, E) 150kPa, F) 200kPa. This change is quantified in Figure 19

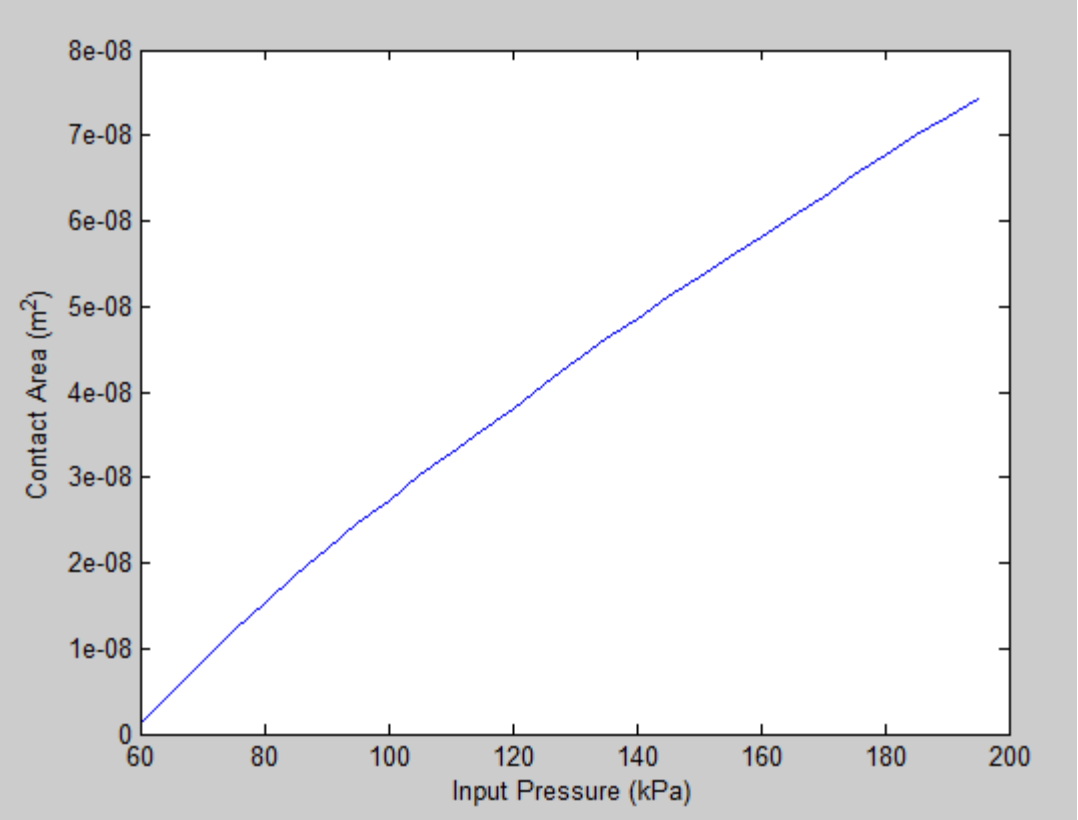

Figure 19: Quantification of the change in contact area as a function of loading pressure.

3.1.3 Crush Pad Remodeling

In order to create a way to apply mechanical insult in a more spatially controlled manner, a 30 µm wide extension was added to the design, as shown in Figure 20. In the first design, the area over which the force which contacts the axon was applied changed as a function of the input pressure. Figure 18 shows how the contact area of the original design changed as a function of input pressure, showing variation in contact area along both the X and Z axis. Thus, in any experiment which would aim to compare the effects increased crushing force on an axon would also have to take into account the accompanying increase in area over which the crush is being applied. Using the redesigned crush membrane, the area of the membrane used to apply the crush

injury any individual axon was designed to be independent of pressure. The PDMS membrane was modeled with 165,000 tetrahedral elements (SOLID185), while the glass substrate was modeled with 15625 tetrahedral elements (SOLID185). Again, a sensitivity study was completed in order to find an optimal meshing density. In this study, the element count was increased until the change in displacement due to the input pressure between increased meshing densities was less than 1%. The upward facing (positive-Y facing) surface of the glass volume was defined as the target surface (TYPE2) for the sake of contact modeling, while the lower (negative-Y facing) surface of the PDMS crushing pad volume was designated as the contact surface (TYPE3).

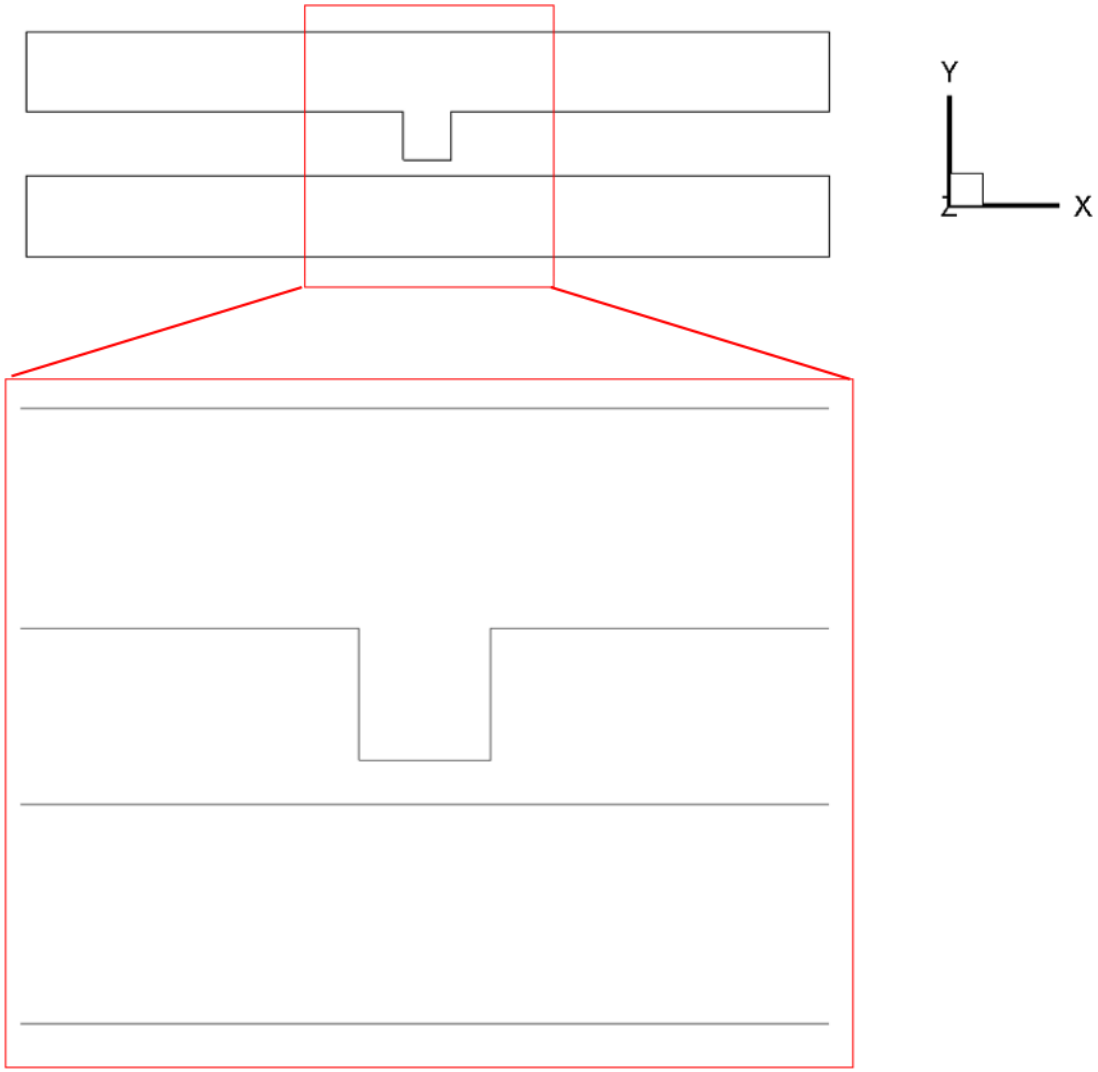

Figure 20: Schematic showing the redesigned axon crushing membrane. Inset shows detail of the crush pad added to the design.

Images from the FEM study showing the deformation of the remodeled crush pad at different loading input pressures can be found in Figure 21, Figure 22, and Figure 23. While there is still an input-pressure dependence on the contact area along the Z axis, the contact area along the X axis is no longer variable, and as such the contact area of the crushing membrane with any given axon will not change as a function of input pressure. Furthermore, Figure 24 shows the

relationship of the deformation of the crushing membrane, shown as the distance between the membrane and glass substrate as a function of the input pressure.

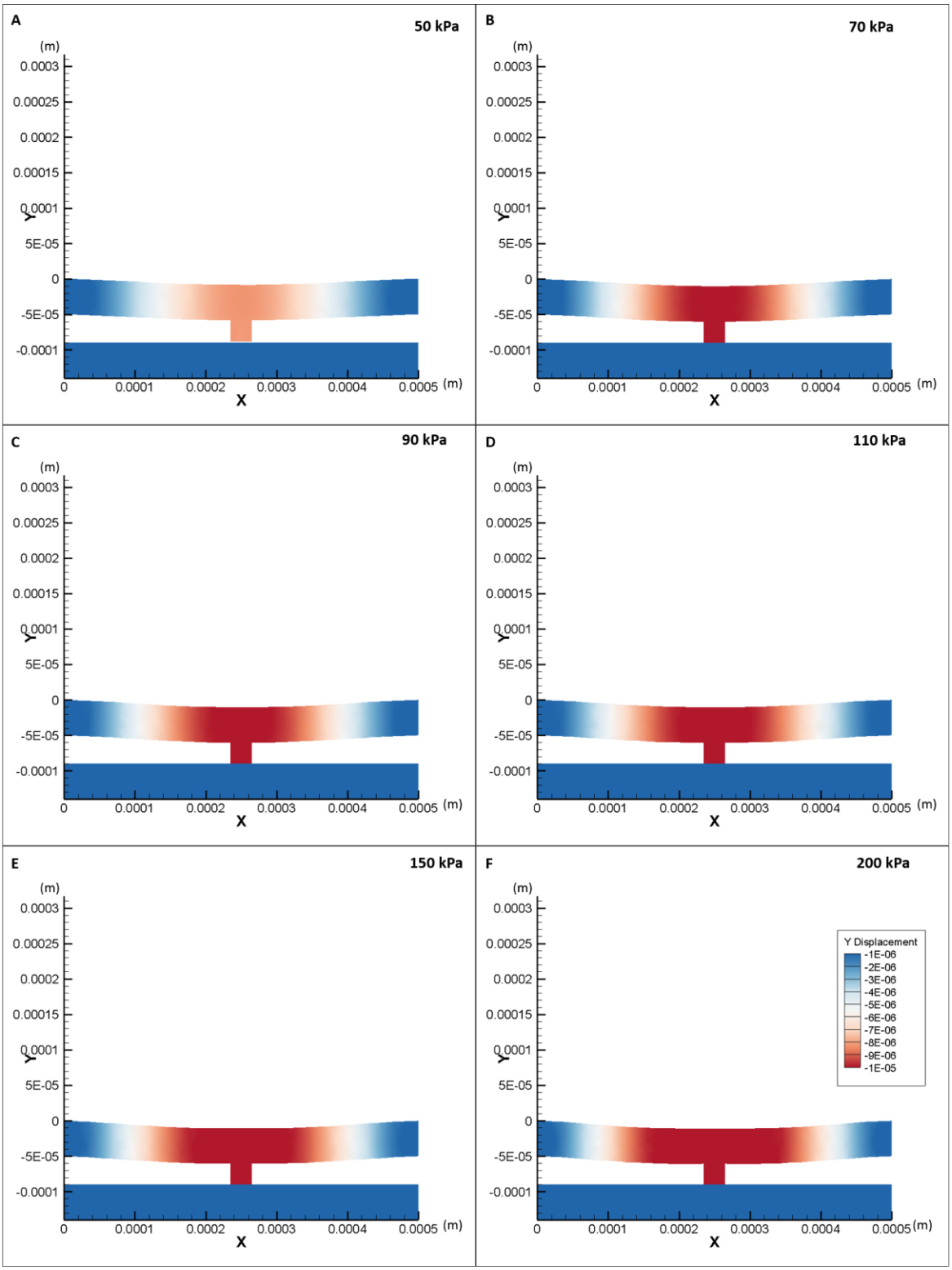

Figure 21: PDMS membrane with crushing pad Y-deformation along the X axis at A) 50kPa, B), 70kPa C), 90kPa D) 110kPa, E) 150kPa, F) 200kPa. Slices taken from the mid-point of the structure to reduce boundary-condition effects.

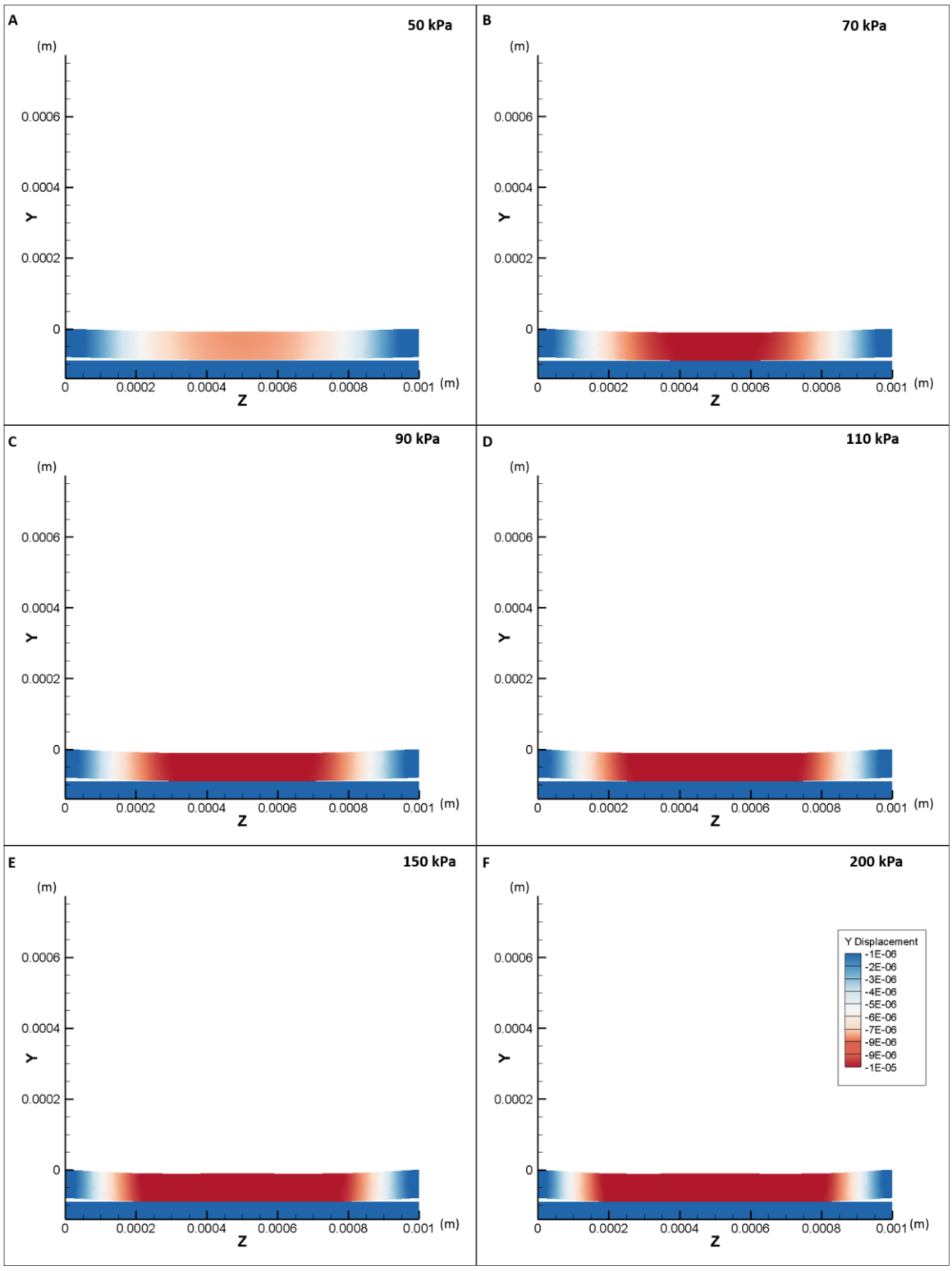

Figure 22: PDMS membrane with crushing pad Y-deformation along the Z axis at A) 50kPa, B), 70kPa C), 90kPa D) 110kPa, E) 150kPa, F) 200kPa. Slices taken from the mid-point of the structure to reduce boundary-condition effects.

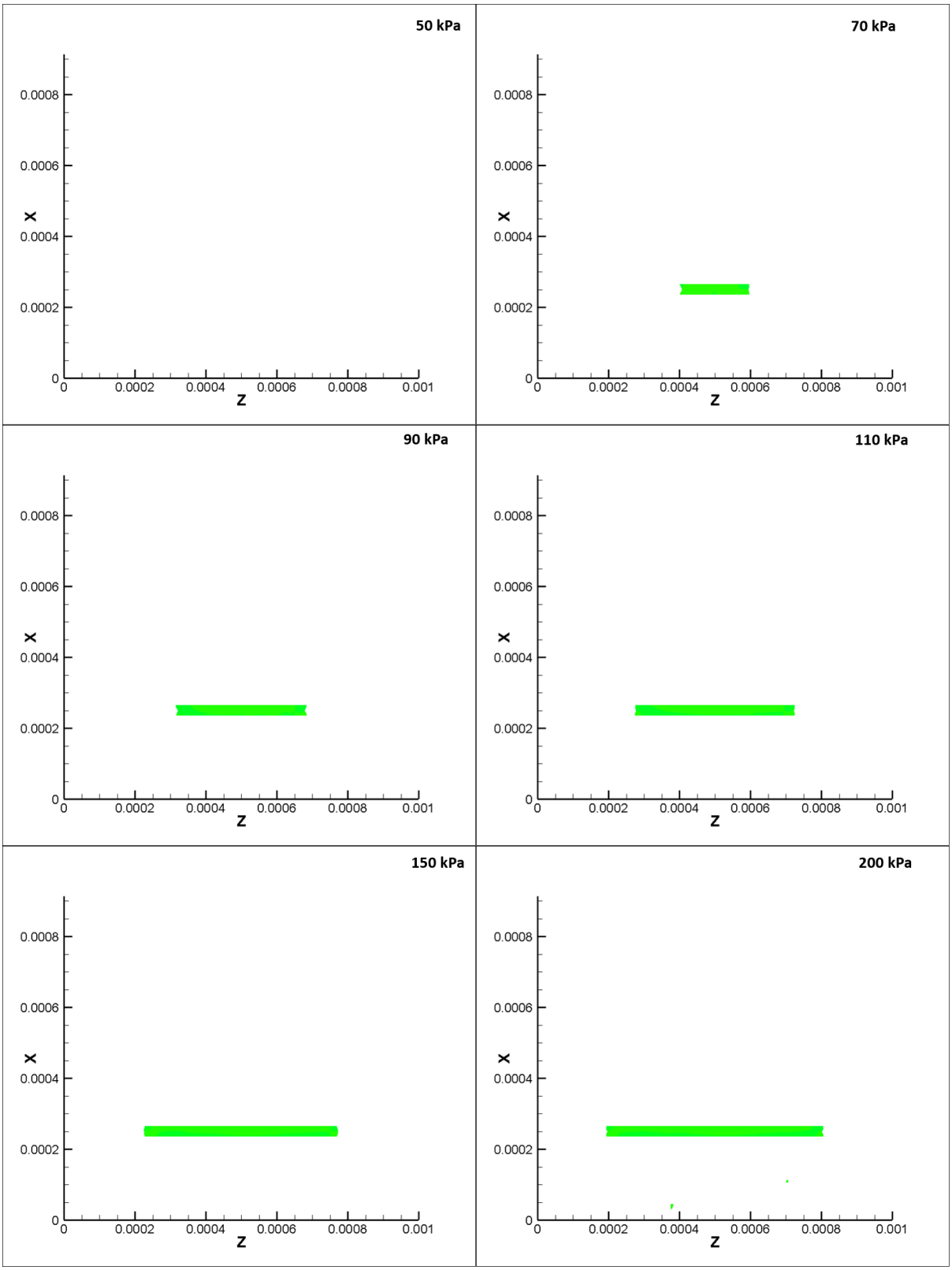

Figure 23: Contact area of PDMS with the glass substrate for loading pressures of A) 50kPa, B), 70kPa C), 90kPa D) 110kPa, E) 150kPa, F) 200kPa.

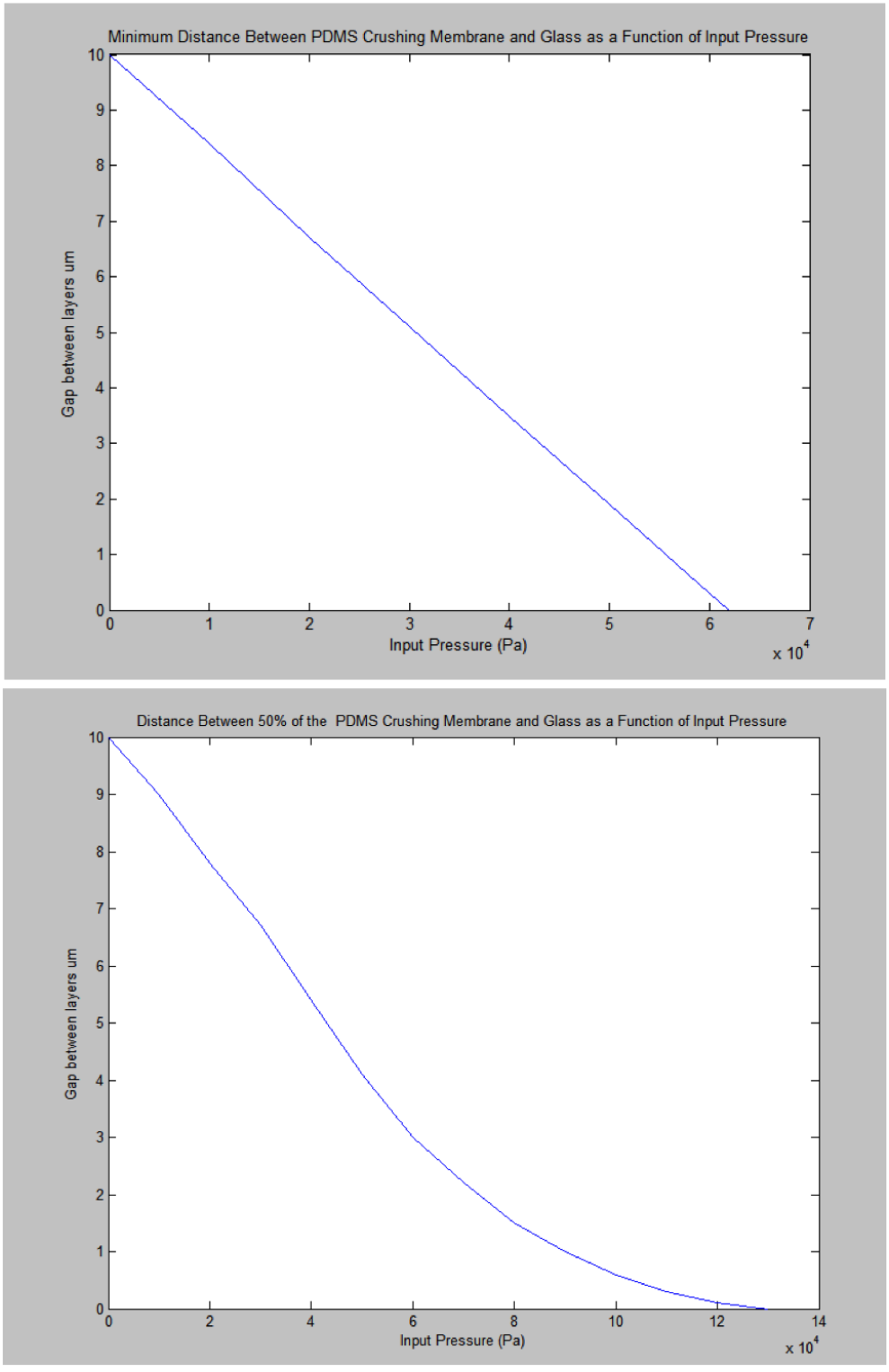

Figure 24: Plots showing (top) the minimum distance between the crushing membrane and substrate, and (bottom) the average distance between of 50% of the length of the crushing membrane as a function of input pressure

3.2 Conclusion

A design which was informed by the literature base of microchannel-based axonal separation devices, as well as finite element modeling was developed. Using these developmental tools as guidelines, the requirements set out in section 3.1 were able to be met.

Chapter 4: Device Fabrication

4.1 Microfabrication

As the ALD was designed with feature sizes on the order of tens of microns, conventional manufacturing techniques were not able to be employed in its fabrication. PDMS replica molding, a process developed and popularized by Whitesides in the early 2000's, was chosen as the method to create the device [60]. This process involved the creation of a patterned silicon wafer, which was used as a master in a molding process. For this technique, PDMS was poured over the mold and allowed to cure. This process transferred the features that were patterned on the wafer into the cured PDMS structure. All microfabrication processing was completed in the cleanroom facilities at the Marcus microfabrication cleanroom of the Institute for Electronics and Nanotechnology at Georgia Tech.

4.1.1 Photolithography

Photolithography is a technique pioneered in the electronics industry for transferring patterns defined by a photomask onto a substrate that has been coated with a photo-sensitive material known as photoresist. Briefly, a photomask consisting of a glass plate coated on one side with an opaque (to the wavelength of electromagnetic radiation being used) film such as chromium is used to define the areas of the photoresist-coated substrate which are exposed to a light-source. Depending on the type of mask employed, the pattern may be defined by negative spaces in the film, through the use of a negative mask, or defined by the original pattern, using a positive mask.

4.1.1.1 Photomask Design

The photomasks that were used in the photolithography portion of the microfabrication process (see Appendix A) were designed using AutoCAD (Autodesk, Inc.), and were submitted to the Mask Shop of the Institute of Electronics and Nanotechnology at the Georgia Institute of Technology for printing. The photomasks were printed on 5 inch square glass plates using a Microtech Laserwriter LW405, with chromium as the masking material. All mask features were two orders of magnitude larger than the minimum writable feature size able to be written by the LW405, ensuring that the design was able to be faithfully printed to the glass. The polarity of the photomask was dark-field, and the parity chosen was "Right Read Chrome Down".

Three different photomasks were used in the fabrication of the two master molds required to fabricate the device. Two photomasks were needed to make the mold which comprised the cell seeding area, microchannel array area, and axon crushing pad, and one mask was used to create the mold which defined the inflation chamber and access ports.

In most cases, a process flow will include coating a substrate, typically a silicon wafer, with a photoresist, and exposing the wafer to light of a wavelength corresponding to the active band of the photoresist. This exposure causes the photoresist to crosslink, forming a permanent bond with other exposed regions, as well as to the substrate wafer substrate. A typical photolithography process is shown in Figure 25. The wafer is subsequently washed in a developer solution where the remaining uncross-linked resist is rinsed away, leaving only the pattern defined by the photomask.

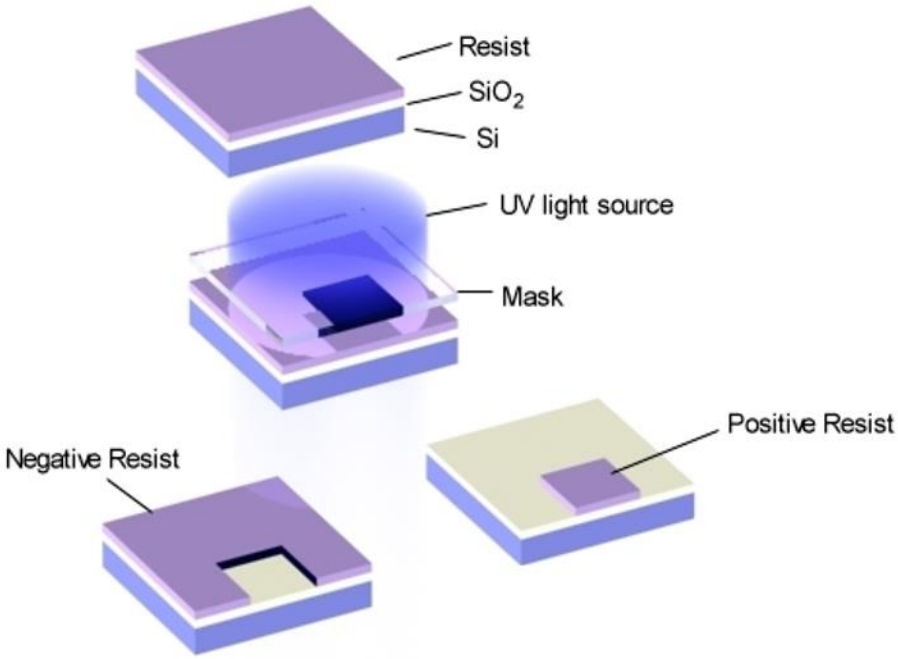

Figure 25: Basic steps in Photolithography. Image from [61]

As the design included features of multiple heights, a photoresist capable of creating layers of a wide range thicknesses was required. 2000 Series SU-8 negative photoresist (Microchem) was chosen to fill this role for its widespread use in multiple height-step designs across wide range of heights. Though not every feature size is capable of being produced from the same SU-8 formulation, all features were capable of being created using compatible formulations.

4.1.1.2 Photolithography Process Flow

The parameters for all of the steps in the photolithography process can be found in Table 5. Prior to the UV exposure step, SU-8 2007 was uniformly distributed to a layer height of approximately 10 µm using a photoresist spinner. (BLE-SussMicrotec), and excess photoresist was allowed to evaporate off during a soft-bake step on a hotplate. The coated wafer was then exposed to a

photoresist-thickness dependent dose of UV light through the mask which defined the pattern of the first layer of the device. The wafer was then exposed to a post-exposure bake on a hot-plate to further assist in the cross-linking process. A layer of SU-8 2015 was then distributed across the wafer, followed by a pre-exposure bake on the hot plate. The second layer mask was then aligned with the alignment crosses defined by the first exposure step, and exposed a second time with a thickness dependent dose of UV radiation, followed by a post-exposure bake. The wafer was then submerged in a bath of SU-8 developer solution (Microchem) and agitated for several minutes. The wafer was then removed from the developer solution, and rinsed with isopropyl alcohol. If there was any white residue, the wafer was placed in a new bath of fresh developer, and agitated for an additional minute, removed, and rinsed; this process was repeated until no white residue remained after the developer step. This process was then repeated using SU-8 2050 to create the mold which defined the control layer of the device. The parameters are based on data sheets for the SU-8 formulations which were used, and modified as needed to achieve the desired results [62].

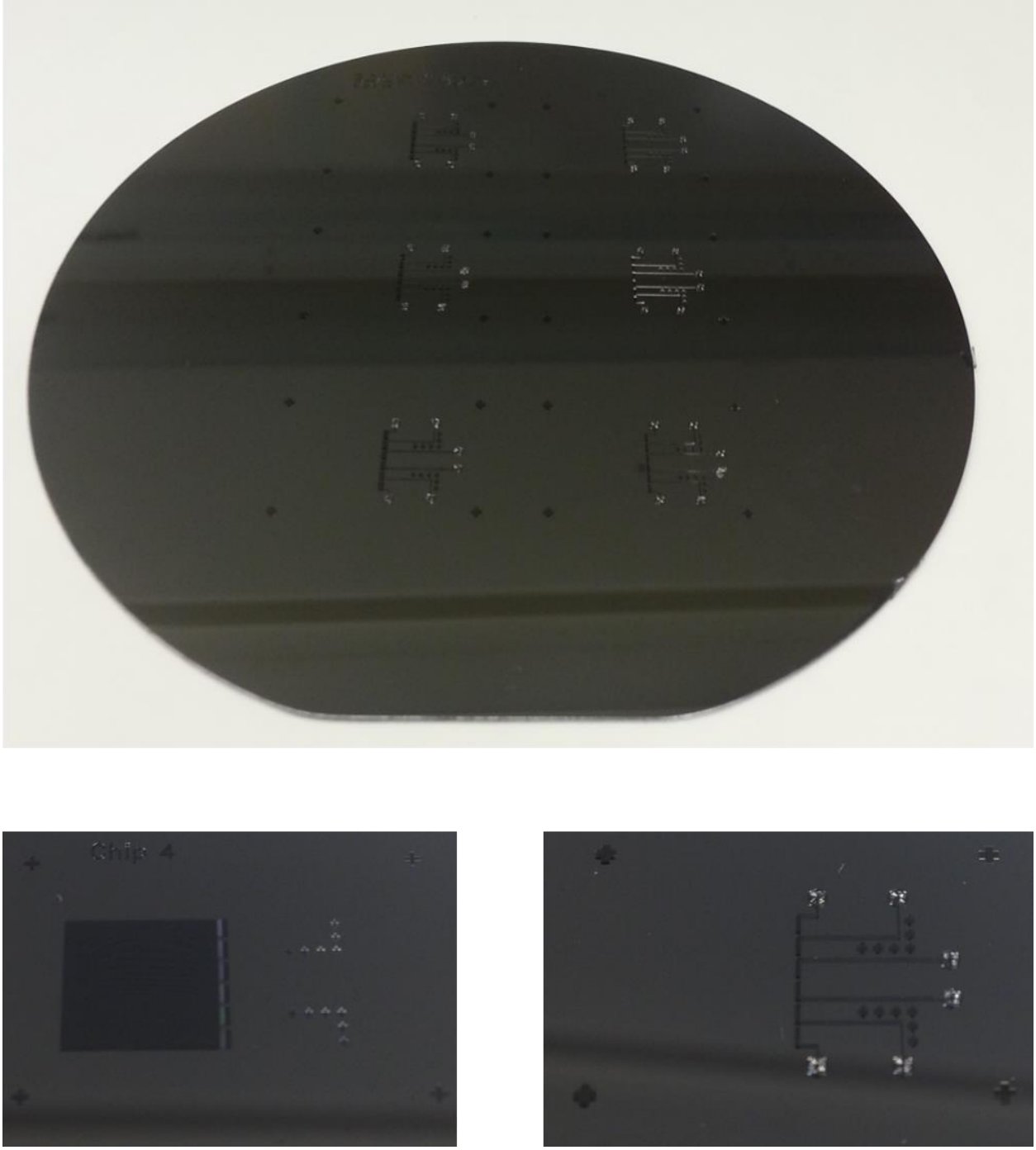

Figure 26: Top: A photograph of the patterned silicon wafer defining the inflation bladder access ports. Bottom Left: Photograph detailing the mold of the cell seeding area, microchannel arrays, and axonal injury compartments. Bottom Right: Photograph detailing the mold of the inflation bladder area, as well as access ports.

Table 5: Processing parameters for SU-8 2007, 2015, and 2050

Feature Height	SU-8 Formulation	1st Spin Step	2nd Spin Step	Soft Bake	Exposure Energy	Post-Exposure Bake	Development Time
10 µm	2007	10s @ 500rpm with 100 rpm/s	30s @ 1500rpm with 300 rpm/s	3min @ 95°C	170 mJ/cm^2	4min @ 95°C	3min
30 µm	2015	10s @ 500rpm with 100rpm/s	30s @ 1400rpm with 300rpm/s	4min @ 95°C	210 mJ/cm^2	6min @ 95°C	5min
100 µm	2050	10s @ 500rpm with 100rpm/s	30s @ 1700rpm with 300rpm/s	5min @ 65°C 10min@95°C	270 mJ/cm^2	3min @ 65°C 9min @ 95°C	10min

4.1.3 Contact Profilometry

Contact profilometry was employed to verify the profile height of the features patterned on the silicon master molds. The measurement technique is based upon loading the wafer into a movable stage, bringing a stylus into intimate contact with the silicon wafer, and translating the stage along the direction of the features to be analyzed. This technique was used to ensure that the dimension-critical features of the microchannels were consistently defined.

The profilometer used in this study was the Dektak 150 Profilometer (Veeco), which is capable of resolving differences in height to 4 Å, according to the manufacturer. As for horizontal resolution, the device has a fixed sampling rate of 300Hz – though the translation speed of the mounting stage can be modulated through changing the scan duration or length parameters. Profile scans in this study were designed to allow 36 height samples to be taken per micron of translation.

Table 6: Microchannel array step heights

Feature	Average Step Height of Array	Standard Deviation
Microchannel Array 1	11.58 µm	.81 µm
Microchannel Array 2	11.37 µm	.71 µm
Microchannel Array 3	10.89 µm	.68 µm
Microchannel Array 4	12.32 µm	.44 µm
Microchannel Array 5	12.47 µm	.38 µm
Microchannel Array 6	11.93 µm	.23 µm

4.2 Soft-Lithography

Using the silicon wafer based molds created in the photolithography step, soft-lithography, a technique pioneered by Whitesides *et al.*, was used to form the PDMS devices [60]. This process uses the pattern formed on the silicon and SU-8 wafer during the photolithography step to cast PDMS devices in a replica molding step.

4.2.1 Surface Treatment

Prior to using the master mold, the wafer was surface treated to facilitate easy removal of the PDMS from the mold. This was achieved through the silanization of the wafer surface, as follows: the wafer was placed in a desiccator along with a microscope slide that had 5 drops of a silane compound (Tridecafluoro- 1,1,2,2-tetrahydrooctyl-1-trichlorosilane (Pfaltz & Bauer))

distributed on its surface. A vacuum was then pulled to encourage the evaporation of the silane compound. The wafer was left in the desiccator for 4 hours, allowing for the silane compound to form a monolayer on the wafer.

4.2.2 PDMS Preparation

Prior to being molded, the PDMS elastomer was prepared using a modified version of the manufacturer's suggested protocol, in order to facilitate the bonding of one PDMS layer to another. The ratio of base to curing agent for the first layer was 5:1, while the mixture for the second layer was 20:1 [63]. After the PDMS had been thoroughly mixed for 7 min, the mixed PDMS was placed in a vacuum chamber for 30 min in order to remove the air bubbles that had been introduced into the fluid through the mixing process.

4.2.3 Molding the First Layer

The device was comprised of two layers, and required two soft-lithography steps. The first layer, using the master mold which had been patterned with the microchannels and crushing membrane, was designed to be a PDMS layer 50 μm thick. In order to create a uniform layer of this thickness, the PDMS was spin-coated onto the wafer using a spinner-plate (BLE-SussMicrotec). The PDMS was spun at 4000 rpm for 60 s. This PDMS layer was then partially cured in an oven for 15min at 75℃.

4.2.4 Molding the Second Layer

The second layer, using the master mold of the control layer, was formed by pouring approximately 30 mL of mixed PDMS elastomer over the mold. The PDMS was then allowed to

partially cure in an oven for 90 min at 75°C. The partially cured PDMS was carefully peeled from the mold, and the fluidic access holes were punched using 20 gauge blunt needles.

4.3 Device Assembly

Once the two layers of PDMS were molded in the soft-lithography step, the PDMS slab of the upper layer was cut into individual device components. The lower spin-coated layer was left on the silicon mold. Alignment marks on the lower layer mold, and corresponding marks on the upper layer PDMS device were used to bring the two pieces into contact. The assembled upper and lower layers were then put into the oven overnight (minimum of 8 hours) to complete the curing process, and form a monolithic PDMS structure. After the devices had been fully cured, the wafer was removed from the oven, and each device was cut from the mold. Access ports to the cell culture area of the device were then cut using a No. 11 scalpel. A piece of tape (3M) was then placed on the microchannel side of the device to protect it from debris.

An assembled PDMS device and a microscope slide (VWR) which had been treated via sonication in an ethanol bath were placed in the plasma chamber (Harrick Plasma). The PDMS devices were placed with the microchannel side (the side to be bonded to the glass) facing up. A vacuum pump was run for 90 s to create a vacuum in the oxygen plasma chamber between .1 - 100 Pa. The RF treatment was then applied at maximum intensity for 90 s. After exposure to the plasma, the plasma chamber was rapidly brought to ambient pressure, and opened. The treated PDMS device and microscope slide were then brought into contact in order to form an irreversible bond. The completely assembled device was then put into the oven at 75°C overnight to finish the bonding process. An image of two fully assembled ALDs can be found in Figure 27.

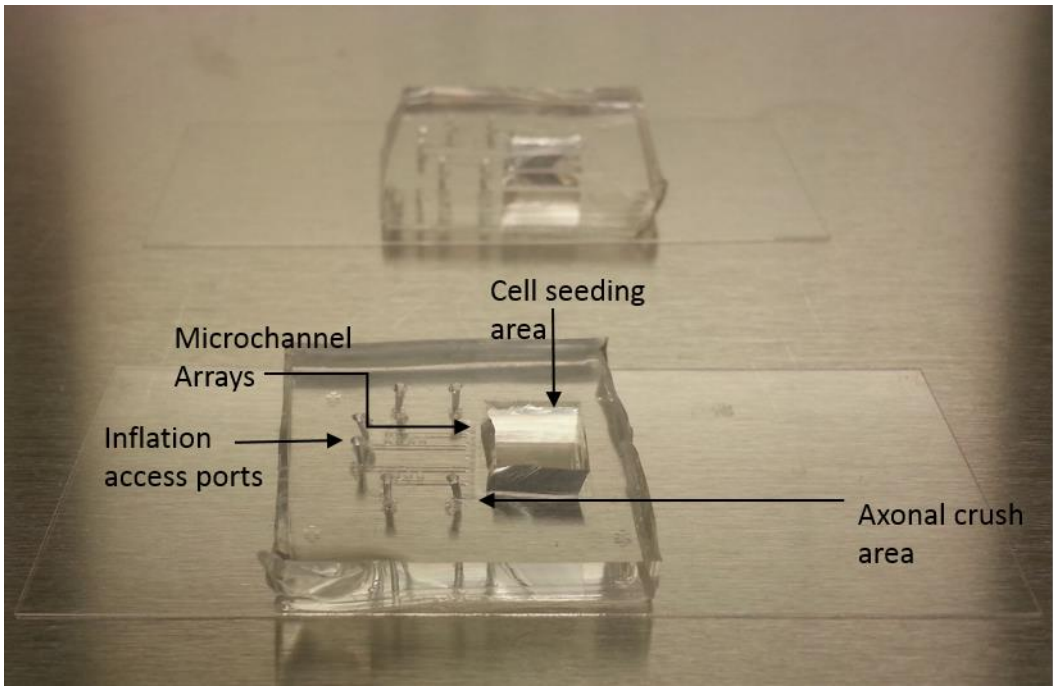

Figure 27: Two fully assembled devices

Chapter 5: Device Characterization

After fabricating the molds to create the ALD, the device needed to be characterized in order show proof of concept. First, to establish the biocompatibility of the device, cells from the P19 cell line were seeded into the device and kept in culture until they reached confluence. Additionally, preliminary inflation tests were done in order to verify the basic function of the axonal crush area.

5.1 Biocompatibility

To test the biocompatibility of the devices, cells were loaded into the cell seeding area of the device and kept in culture. The cell type chosen for the biocompatibility test was the P19 mouse embryonic carcinoma cell line. P19 cells can be maintained in an exponential growth phase until differentiation is initiated, forgoing the need to harvest primary cells to test biocompatibility [64]. This feature, alongside the capability of the P19 cells to be differentiated into neuronal cell types with axonal projections in order to test the ability of the microchannels to separate axons, made the P19 cell line an attractive choice for the study [65]. In retrospect however, the rate at which the P19 cells divided during their growth phase made them difficult to use in the biocompatibility assay, as they would reach confluence within the device in a matter of days – and the culture would begin to quickly deteriorate due to overcrowding soon after reaching confluence.

5.1.1 P19 Cell Culture

Pellets of P19 cells (ATCC), stored in liquid nitrogen, were thawed, and immediately plated in a T75 cell culture (Falcon) flask prepared with 15mL of warmed growth medium, which was then placed in an incubator at 37°C. The growth medium used was Alpha Minimum Essential Medium

(α-MEM) supplemented with ribonucleosides and deoxyribonucleosides (Mediatech), Penicillin-Streptomycin (Hyclone), 7.5% bovine calf serum (ATCC), and 2.5% fetal bovine serum (Hyclone). Cultures were maintained until 90% confluence was reached, typically after approximately 48 hours, and then passaged 10:1.

Prior to passaging, growth medium, phosphate buffered saline (PBS), and trypsin were placed in a heated water bath, and warmed to 37℃. The spent growth medium was aspirated out of the T75 flask, and the cells were rinsed with PBS, which was subsequently aspirated out. 3mL of trypsin (Cellgro) was pipetted into the T75 flask, and allowed to incubate at 37℃ for 5 minutes. 7mL of culture medium was then added to neutralize the trypsin. The mixture was then triturated to yield a single cell suspension. 14mL of fresh growth medium was then added to a new T75 flask, and 1mL of the cell solution from the original T75 was then added to the new flask, and placed in the incubator at 37℃.

5.1.2 Device Seeding

Prior to seeding, all ALDs were autoclaved for sterilization. To prepare the glass substrate for having cells seeded into the ALD, 125 µL of poly-D-lysine (Sigma Aldrich) solution was added to the cell seeding area of the device and allowed to incubate at 37℃ for two hours to provide the cells with an appropriate substrate for cellular attachment [66]. Following incubation, the cell seeding area was twice washed with sterile filtered Milli-Q® water (Resistivity: 18.2 MΩ·cm) to rinse the ALD of excess poly-D-lysine. If the ALD was not immediately seeded with cells, the device was kept in the incubator with sterile filtered Milli-Q® water in the cell seeding area until used.

Using the protocol from section 5.1.1, cells were passaged, and an additional 1 mL aliquot of cell suspension was pipetted into a 15 mL centrifuge tube. The suspension was spun down to a pellet via centrifugation for 5 min. at 1000 rpm, and resuspended in PBS. Cells were then counted using the Scepter™ automated cell counter (Millipore), again pelleted, and resuspended in growth medium. Approximately 1000 cells suspended in 125 µL of growth medium were seeded into each device, for a seeding density of approximately 20 cells / cm^2. After 12 hours, the plated cells were imaged using an EVOS XL inverted microscope (Life Technologies) to observe if the cells had attached to the coated cover slip, as seen in Figure 28. If the cells had not attached, they were imaged at 6 hour intervals until attached. Once the cells had attached, the seeded devices were then placed in sterile bacterial grade petri dishes, which were then flooded with sufficient growth medium to completely submerge the device, in order to allow free diffusion of nutrients into the device from the bulk medium. Medium in the petri dish was changed every two days.

5.1.3 Results

P19 cells were observed to attach and proliferate on the ALD, showing preliminary evidence of biocompatibility, which is in line with previous studies which make use of PDMS and glass based devices. Though the P19s would attach and proliferate on the ALD, they died off once they had reached confluence. Figure 28 shows the timeline that the cells seeded in ALDs took during the experiments. This progression was also seen in cultures of control P19s which had been seeded at similar densities in 24-well plates on poly-d-lysine coated cover-slips.

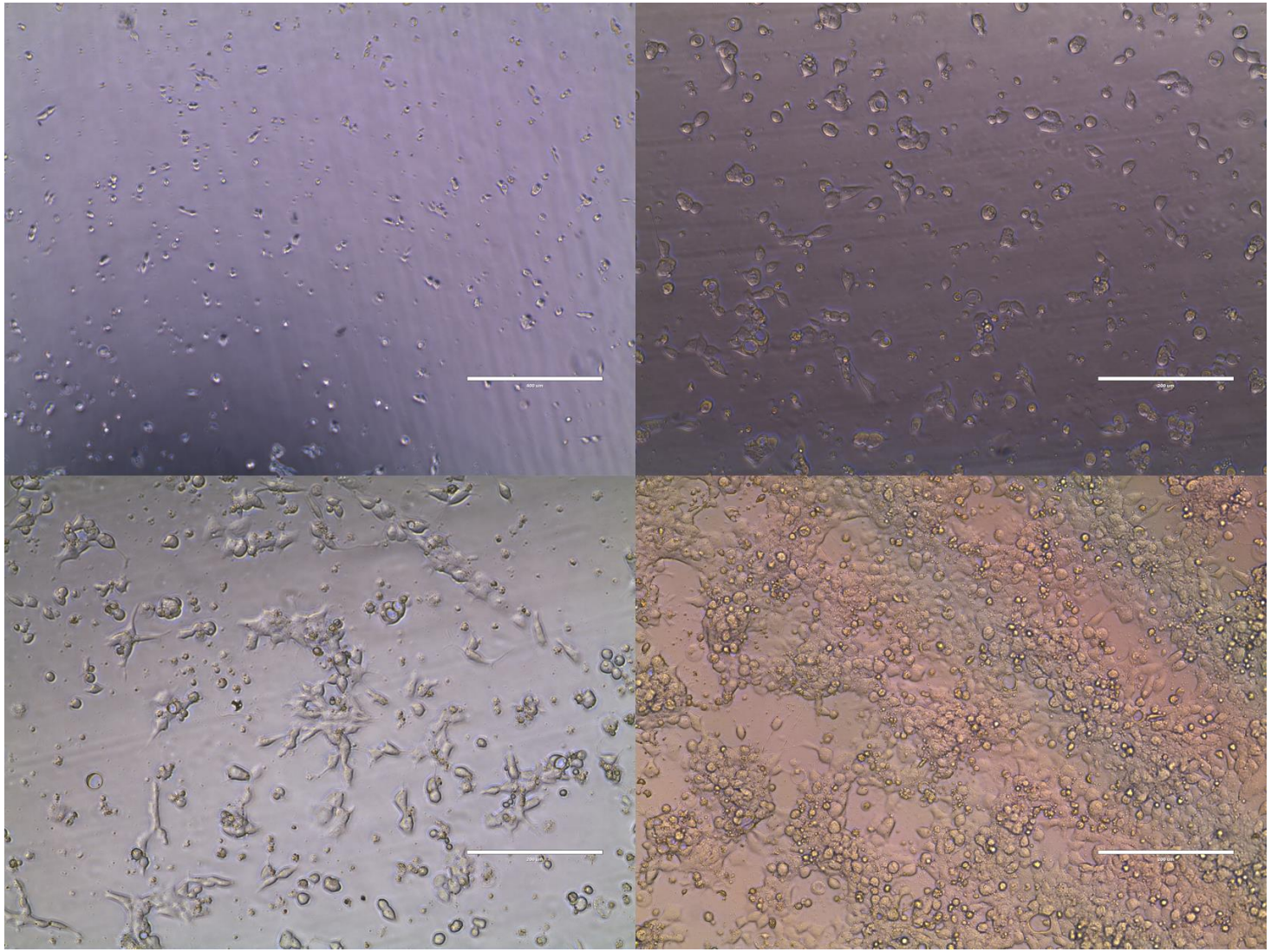

Figure 28: Images of attached P19 cells in the ALD at (Top Left) 12 hours, (Top Right) 24 hours, (Bottom Left) 48 hours, (Bottom Right) 72 hours. Scale bar 200µm

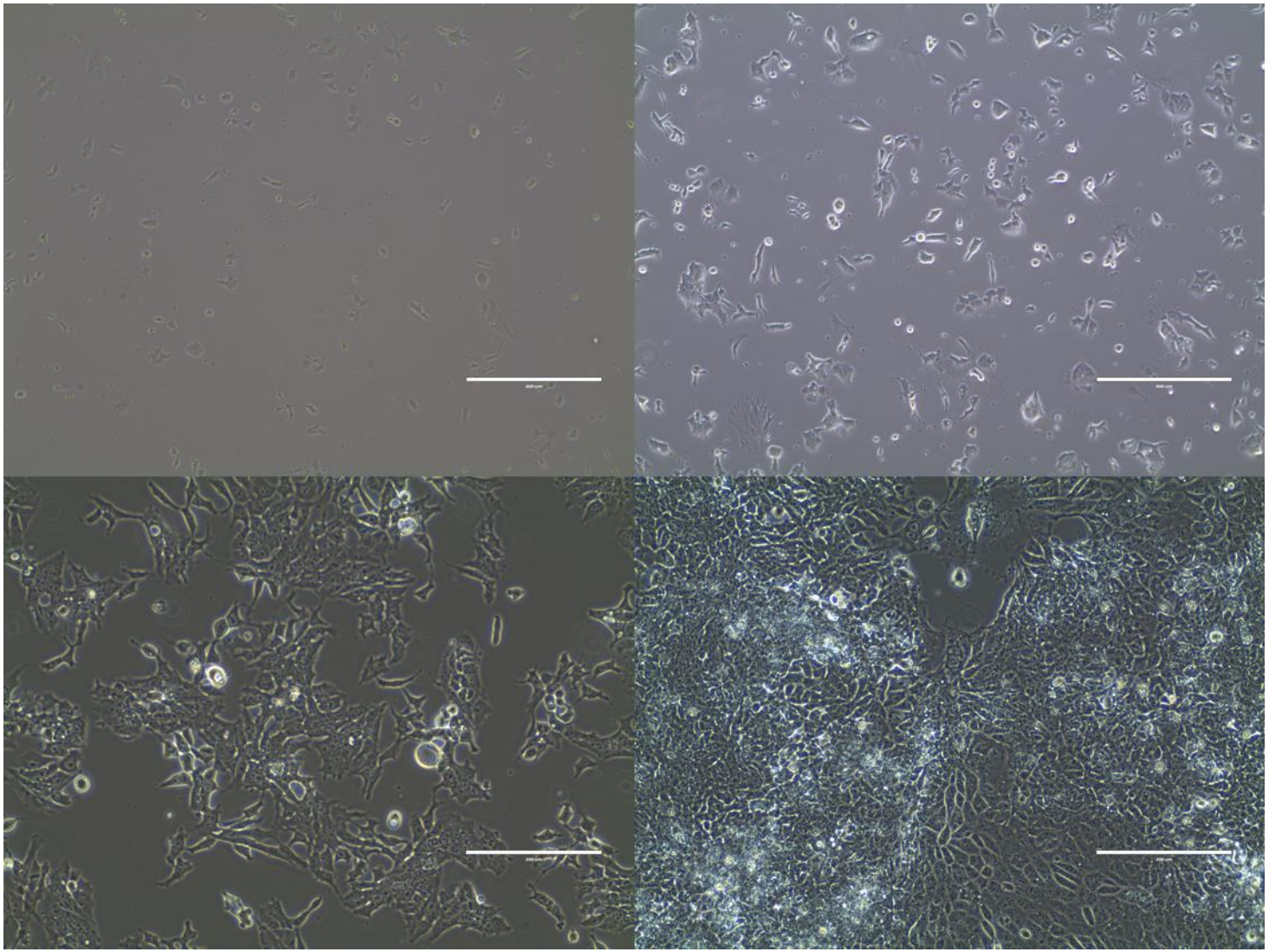

Figure 29: Images of attached P19 cells in 24-well plates at (Top Left) 12 hours, (Top Right) 24 hours, (Bottom Left) 48 hours, (Bottom Right) 72 hours. Scale bar 200µm

5.1.4 Live / Dead Staining

Live/dead fluorescent staining was performed using the Blue/Green ReadyProbes® Cell Viability Imaging Kit (Life Technologies). The NucBlue® Live reagent stained the nuclei of all cells, and was detected with a DAPI filter. The corresponding NucGreen® dead reagent stained only the nuclei of dead cells; and was detected with a FITC/GFP filter. Fluorescent imaging was performed using a LSM 700-405 Confocal Microscope (Zeiss) in the Microscopy Core Facilities of the IBB. Image processing was done with Zen Lite 2012 Blue Service Pack 2 (Zeiss).

To stain the cells, 4 drops of NucBlue®, and 1 drop of NucGreen® stain were added to 4 mL of the growth medium, and mixed in a vortex mixer. The old growth medium in the ALD was aspirated out, and 125 µL of the freshly mixed medium and stain solution was pipetted into the cell seeding area. The device was then placed in the incubator at 37℃. After a 30 minute incubation period, the device was taken to be imaged.

5.1.5 Results

Figure 30 shows the results of one of these experiments after 72 hours of being in culture in an ALD, as well as an image taken at 96 hours which shows the decline of the culture. Again, this progression was also seen in cultures of control P19s which had been seeded at similar densities in 24-well plates on poly-d-lysine coated cover-slips, which can be seen in Figure 31.

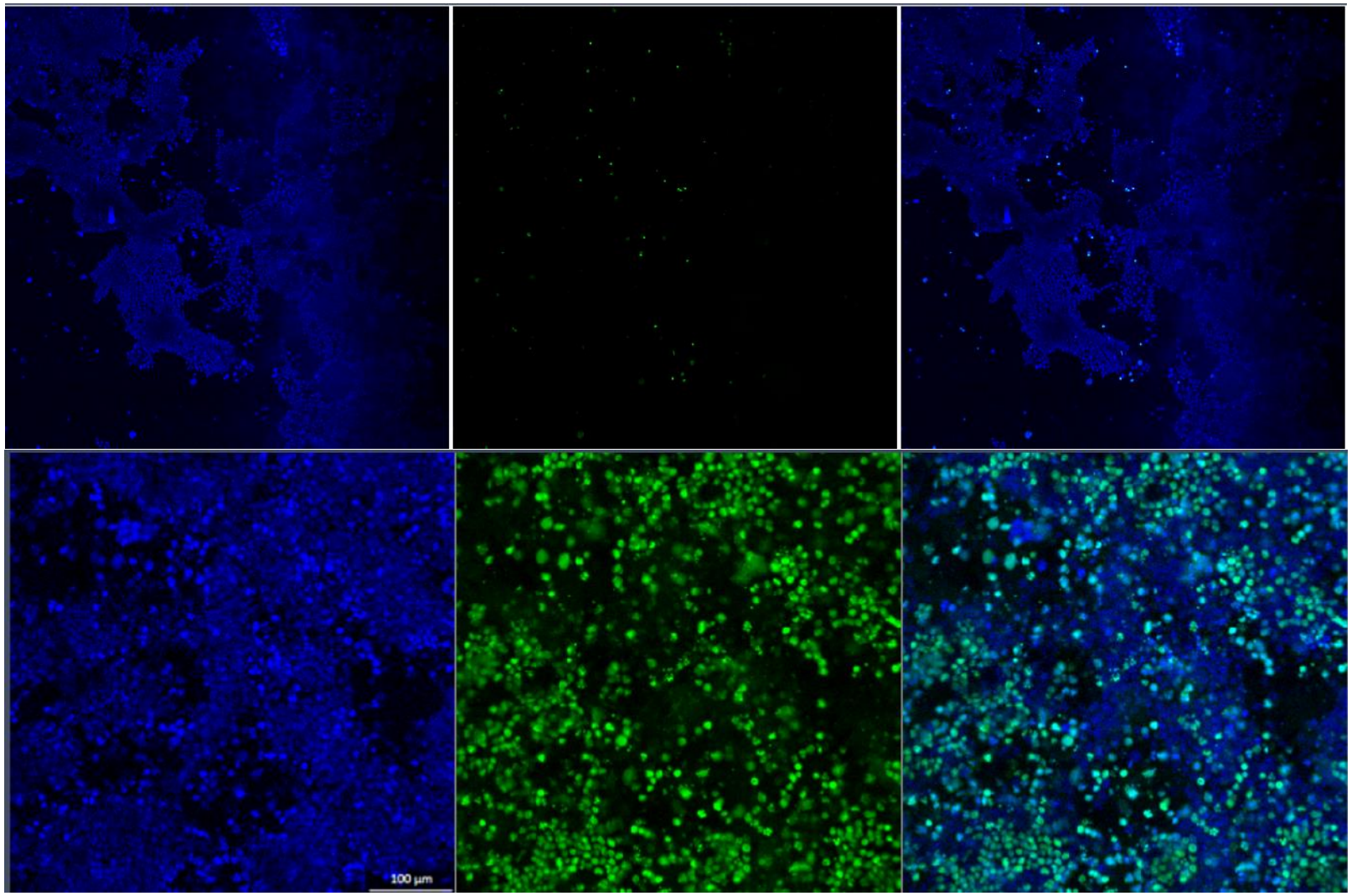

Figure 30: Fluorescent images at 10x of an ALD loaded with cells which had been incubated with the Live / Dead staining kit after 72 (top) and 96 (bottom) hours. (Left) Shows all nuclei stained with NucBlue®), (Middle) the nuclei of dead cells stained with NucGreen ® and (Right) shows a merged image. Scale bar: 100 µm

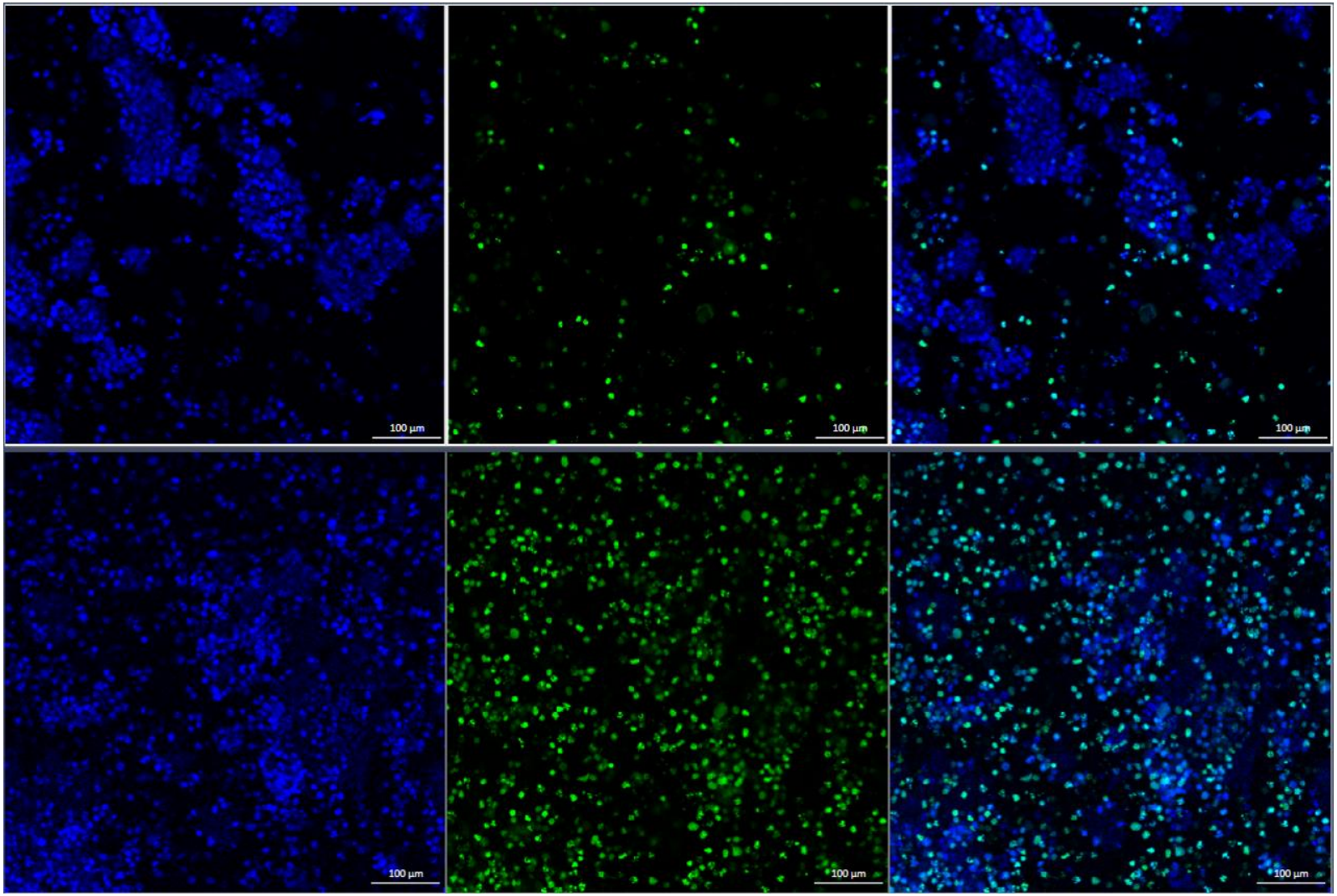

Figure 31: Fluorescent images at 10x of an ALD loaded with cells which had been incubated with the Live / Dead staining kit after 72 (top) and 96 (bottom) hours. (Left) Shows all nuclei stained with NucBlue®), (Middle) the nuclei of dead cells stained with NucGreen®, (Right) shows a merged image. Scale bar: 100 µm

5.1.6 P19 Differentiation

In order to attempt to characterize the cell compartmentalization function of the microchannel arrays, P19 cells were differentiated into neural cells and seeded into ALDs. P19 cells which are grown in bacterial grade petri dishes form cell aggregates known as embryoid bodies (EB). When the EBs are treated with all-trans-retinoic acid (RA) over the course of a 4 day protocol, the cells differentiate into neural cells.

The following protocol was implemented in order to differentiate the P19 cells into neural cells [67] [68]:

Day 0: undifferentiated P19 cells were plated at a density of $1x10^6$ cells in 10mL of differentiation medium (DM) on bacterial grade petri dishes to encourage the differentiation process. DM is composed of α-MEM, 5% FBS, and a Penicillin-streptomycin solution (Hyclone). After the cells were seeded, 1 µl of 5 µM RA (Sigma Aldrich) was added to the petri dish. The petri dish was then placed in an incubator at 37℃ for two days.

Day 2: The contents of the petri dish were then transferred into a 15 mL centrifuge tube (Corning), and the EBs were allowed to settle to the bottom for 30 min. The old medium was then aspirated off, and replaced with 10 mL of fresh DM, transferred to a new petri dish, and supplemented by 1 µl of 5 µM RA. The dish was then allowed to incubate for an additional two days at 37℃.

Day 4: The contents of the petri dish were transferred into a 15 mL centrifuge tube, and allowed to settle for 30 min. The DM was then aspirated off, and the EBs were washed in

5 mL of α-MEM to remove both the serum and RA. The α-MEM was then aspirated off, and 2 mL of trypsin was then added to the tube, and allowed to sit for 5 min. 4 mL of GM was then added to neutralize the trypsin and the cells were triturated, resulting in a single-cell suspension. The cells were then centrifuged for 5 min at 1000 rpm to yield a pellet, and subsequently resuspended in 4 mL PBS. The resuspended cells were then counted, pelleted, resuspended in growth medium and seeded on sterile, poly-d-lysine treated ALDs at a density of 1000 cells per 125 µL of growth medium. Control cultures were seeded at similar densities in 24 well plates on poly-d-lysine coated cover slips.

5.1.7 Differentiated P19 Cell Experiments

While the differentiation protocol did result in the differentiation of a population of P19s into neuronal cell types (see Figure 32), the subpopulation of P19s which did not undergo differentiation continued to proliferate. The continued proliferation of these undifferentiated cells resulted in a mixed culture of neuronal like cells and base P19 cells, as seen in Figure 33.

As the majority of the cells continued to proliferate, the culture followed the same progression to over-confluence and death within 96 hours of being seeded in the ALD post-differentiation as did the undifferentiated P19. An additional consequence of the cells continuing to proliferate was that the axons would only migrate as far as the next group of cells, preventing them from entering the microchannel array.

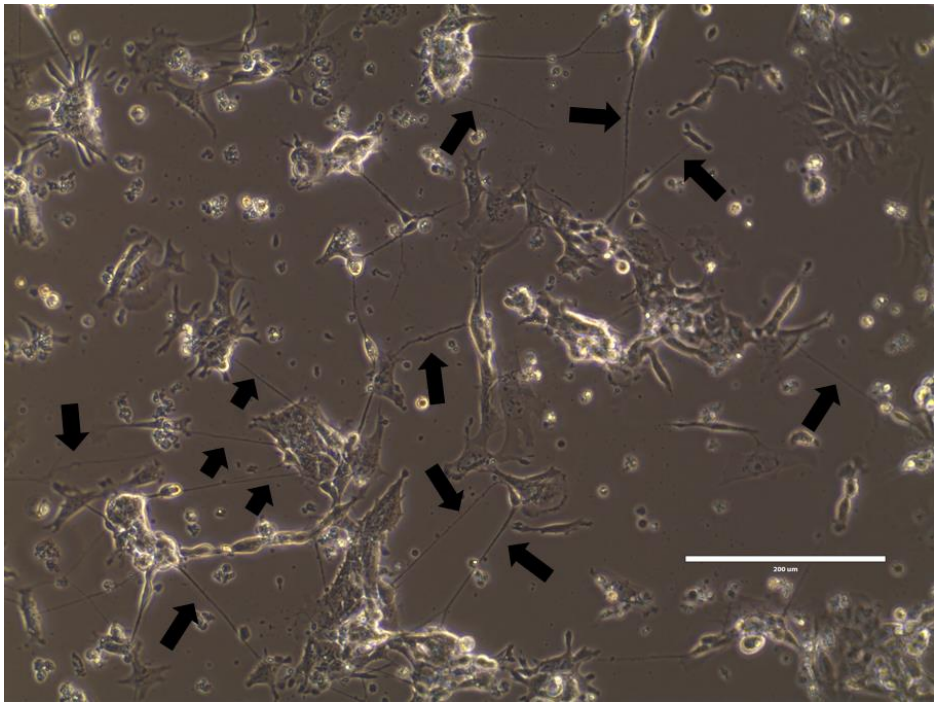

Figure 32: 20x micrograph of P19 cells in an ALD 2 days after the end of the differentiation protocol. Black arrows mark axon-like projections. Scale bar 200 µm.

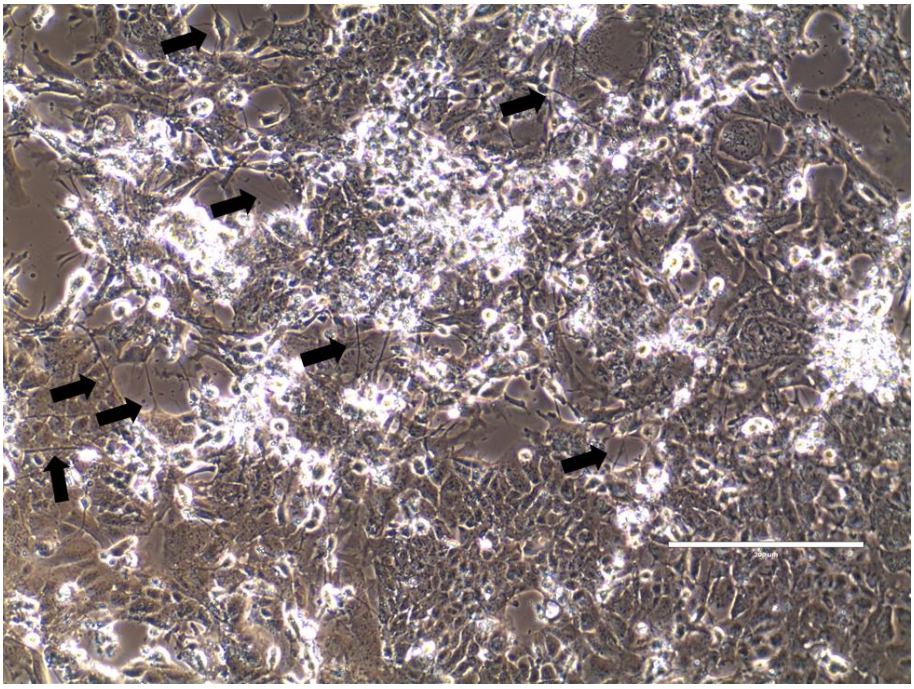

Figure 33: 20x micrograph of P19 cells in an ALD 4 days after the end of the differentiation protocol. Black arrows mark axon-like projections. Scale bar 200 µm.

5.1.8 Conclusions

The ALD was shown to be biocompatible, allowing cells to attach and proliferate in the device. Unfortunately, the cell line chosen was not a good model to study long-term biocompatibility, as the culture proliferate quickly, yet would die off soon after reaching confluence in the small cell culture area. Furthermore, the results of the experiments to characterize the efficacy of the microchannels were inconclusive. Again, this could be attributed to the cell line chosen for the experiments, as only a portion of any culture could be differentiated into the neural cell type.

5.2 Membrane Deformation

5.2.1 Preliminary Deformation Test

A preliminary experiment was conducted to observe the deformation of the axonal crushing area, as well as to test the bond between the two PDMS layers which composed the crushing membrane. For this test, an assembled device was connected to a syringe filled with DI water via Tygon® tubing (Fisher Scientific). The ALD was placed on an EVOS XL inverted microscope, and imaged through the glass coverslip. When pressure was applied, the crushing membrane came closer to the plane of focus of the microscope, as shown in Figure 34. This result showed both that the PDMS bonding protocol was sufficient to create the pressure deformable membrane, and that the crush membrane deformed downward into the axonal crush area.

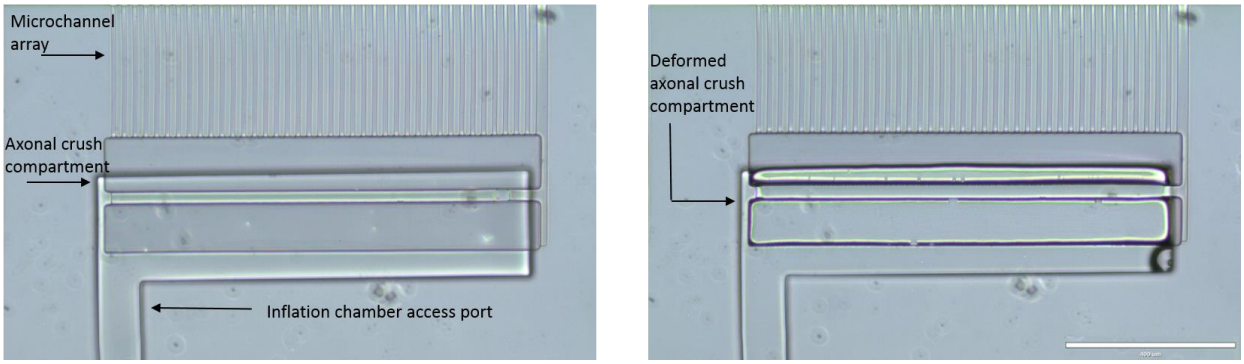

Figure 34: Inflation testing of the axonal crush area showing the pre-inflated state (left) and inflated state (right). In the image on the right, the outline of the axonal crush compartment becomes more in focus as it is deformed downward, closer to the plane of focus of the microscope. Scale bar is 400 µm.

5.2.2 Membrane Deformation Characterization Attempt

An experiment to characterize the deformation of the crushing membrane as a function of input pressure was attempted late in the project. To this end, a similar experimental set-up as the

experiment described in Section 5.2.1 was attempted, with the change that the fluid loaded into the syringe used to pressurize the inflation chamber was fluorescein instead of DI water. Further, to measure the deformation due to the injected fluorescein, the ALD was imaged through the glass coverslip using a Zeiss LSM 700-405 Confocal Microscope.

The aim of the experiment was to measure the downward deflection of the crushing membrane by taking Z-stack images of the crushing membrane under different input pressure levels. This experiment was unsuccessful due to a design oversight which prevented the fluorescein from being loaded into the inflation chamber. As there was only a single input port to the inflation chamber, there was no way to displace the air which was in the chamber prior to applying pressure. Thus, there was no way to load the fluorescein into the device for imaging.

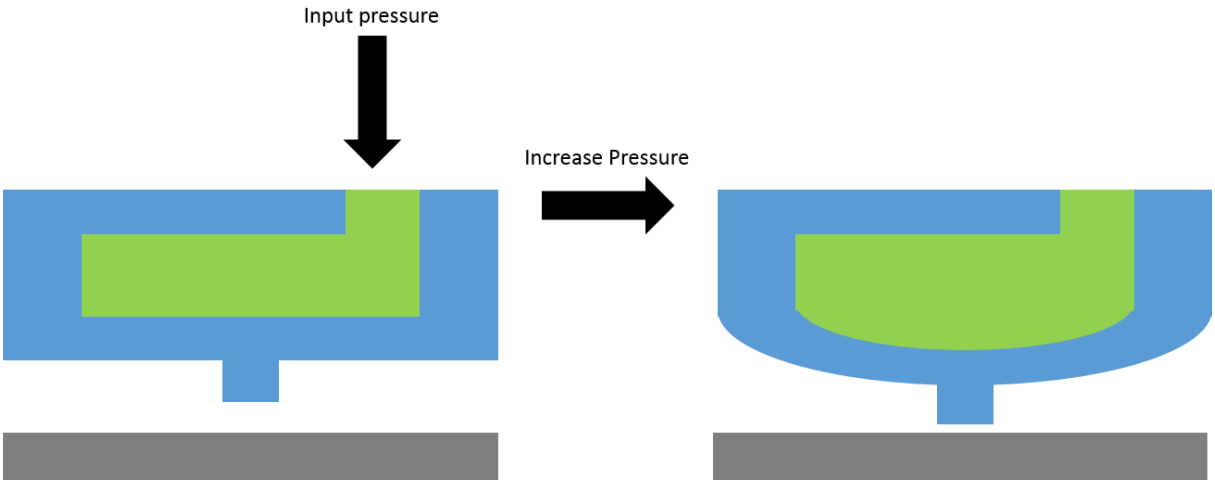

Figure 35: Schematic of characterization experiment. A Z-stack image would be taken at each pressure to measure the change in downward displacement due to the pressure.

A further experiment, undertaken in the last days of the project, was attempted to correct this design oversight. A glass microneedle was used to puncture a hole in the inflation bladder, creating a second fluid port to allow fluorescein loading. This method both failed to create a

reliable seal between the inflation chamber and the microneedle, and compromised the fragile structure of the inflation chamber.

Chapter 6: Recommended Future Work and Conclusions

6.1 Recommended Future Work

6.1.1 Characterization of the Axonal Crushing Compartment

The deformation of the crushing compartment as a function of input pressure remains to be characterized. As stated in the Chapter 5, the first round of experiments to this end was unsuccessful, due to not accounting for the fact that the air within the device prior to inflation would need to be displaced in order to load the area with fluorescein. A method to work around this would be to redesign the experiment, and load the lower chamber of the axonal crush compartment (shown in pink in Figure 36) with fluorescein. Additionally, a new master mold, with an additional fluid handling port to access to the inflation bladder could be manufactured in order to attempt the experiment as originally envisioned. This additional port would allow for the escape of the air from the bladder during the fluorescein loading process. This addition to the design can be seen in Figure 36. The necessary modifications to the photomask to implement this alteration can be seen below in Figure 37.

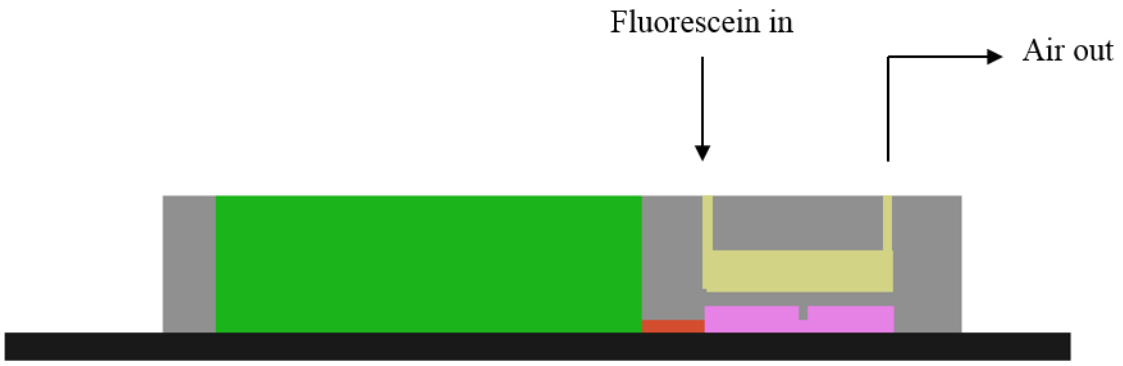

Figure 36: Schematic of the ALD with the additional fluidic access port to allow for deformation characterization experiments.

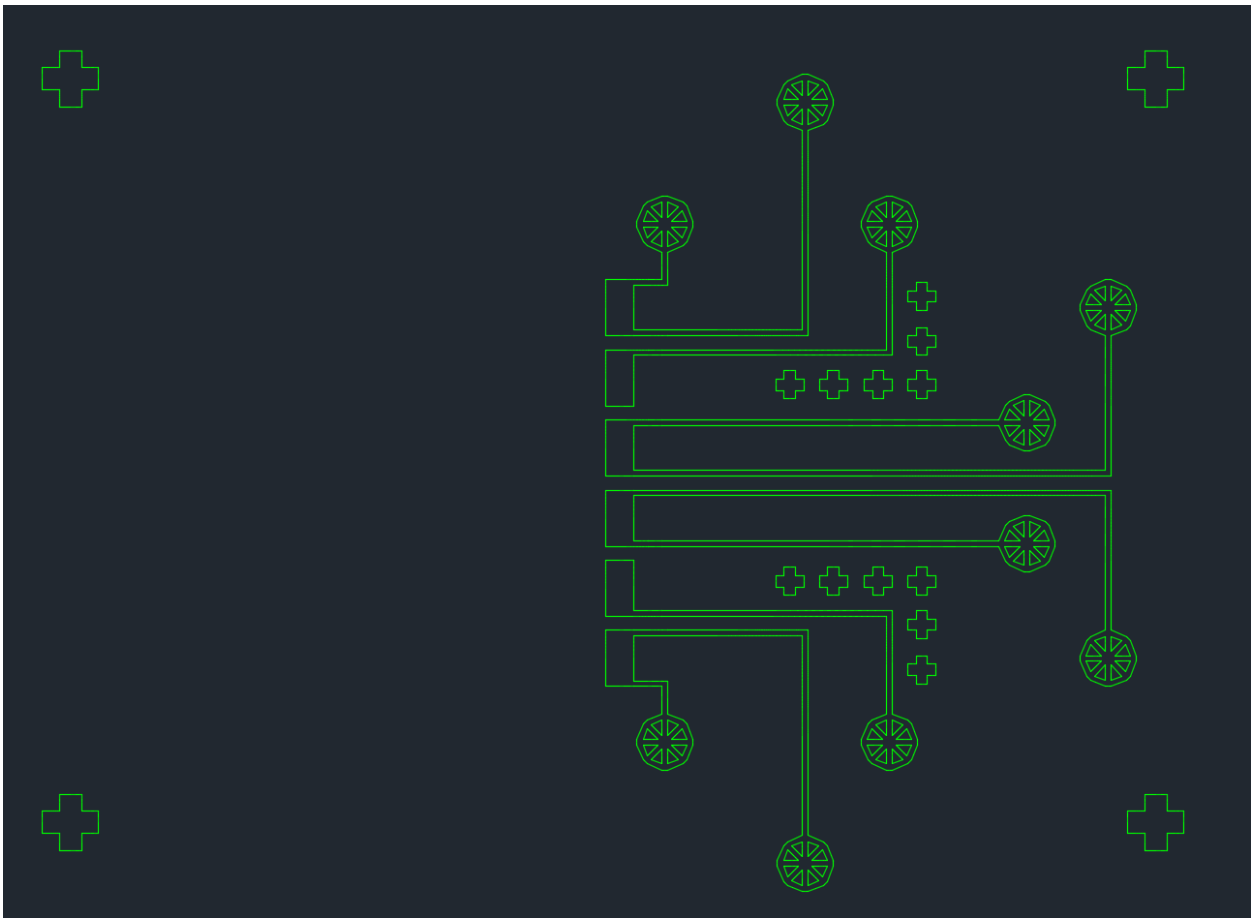

Figure 37: Altered photomask for defining the inflation layer and fluid handling ports which would enable the deformation characterization experiments. The outer two, and inner two deformation chambers have been modified to allow for two fluidic ports.

Though confocal microscopy is a powerful technique for forming 3-D images on the scale of several microns, the axial (z-direction) resolution is limited by several factors. Specifically, the size of the pinhole through which the light passes, along with the magnification and numerical aperture (NA) of the optics, influence the optical (Z) section thickness, and hence the Z-direction image resolution. Practically, using a high NA oil-immersion optical system, high magnification, and a small pinhole aperture, it can be expected to achieve a slice thickness from .856 - 1µm

[70]. This may limit the ability of the confocal approach to characterize the operation of the crushing device.

6.1.2 Validation of the Microchannel Array

In addition to the characterization of the PDMS deformation, the ability of the microchannels to reliably separate the neuronal cell body from the axon remains to be established. During this project, it was shown that the P19 embryonic carcinoma cell line is capable of being differentiated into neuronal cell types, but the differentiated populations achieved in this experiment did not contain enough successfully differentiated cells to observe axons entering the microchannel region.

Thus, it may be fruitful to use primary neuronal cultures to validate the function of the microchannels. It would be advisable for the microchannel function to be first assessed through the use of a neuronal cell type other than RGCs, due to the difficultly in harvesting, purifying, and culturing primary RGCs. Hippocampal or cortical neurons would be a good test neural type before investing resources into experimentation with primary RGC culture [51].

In addition to observing axonal projections migrating along the microchannels, immunocytochemistry should be used to verify that the projections are indeed axons, and not other cellular components. MAP2 (microtubule associated protein) and tau, axonal specific proteins which stabilize the structure of the axon, could be used as positive markers. Additionally, GFAP, glial fibrillary acidic protein, could be used as a negative control stain to show that the cells are indeed neuronal, and not other central nervous system-associated cell types, such as astrocytes.

Depending on the results from this experiment, the dimensions of the microchannel array may need to be altered. For example, if the percentage of microchannels occupied by multiple axons is large, the height of the channels could be changed by creating a new master mold that would result in a smaller microchannel height, or the width of the channels could be changed by altering the channel dimensions in the photomask design.

6.1.3 Axonal Crush Experiments

After the function of the axonal crushing membrane and microchannel portions of the ALD have been characterized, the axonal crush experiments could be performed. These experiments will attempt to correlate the deformation of the axonal portion of RGCs (or other neural cell type) with cellular dysfunction. To appropriately characterize axonal deformation, each ALD used in experimentation would need to have the axonal crush chamber characterized, enabling the deformation of the axon to be inferred from the membrane deformation, which is correlated with the input pressure applied.

One way to assess the damage to a given axon is by tracking of transport of molecules along the axon through the use of fluorescent markers such as Mitotracker Green FM ® and Tubulin Tracker® (Invitrogen) for mitochondria and tubulin, respectively [45].

6.1.4 Electrophysiology and Crush

Another round of experimentation that could be enabled with the ALD is the investigation of the effects of axonal mechanical insult on the electrophysiological function of the neuron. One way to do this sort of assessment would be to use a microelectrode array as the cell culture substrate, replacing the glass coverslip. If there were multiple electrodes running perpendicular to the axis

of the microchannels, the changes due to mechanical insult in how action potentials are transmitted along the axon could be ascertained. Information with regards to the effect that the insult has on the amplitude, frequency and conduction velocity of the action potential could be obtained from this experimental set up.

Electrophysiology experiments could also be undertaken via patch-clamping. This technique involves using a glass micropipette which is embedded in the cell membrane to directly measure the potential of the cell membrane of the cell of interest.

6.2 Conclusions

The main objective of this work was to design, fabricate, and characterize a device for use in axonal loading experiments. To this end, a set of Specific Aims (SA) was laid out to act as milestones. This section restates the SAs, and assess whether or not they were met.

6.2.1 Specific Aim 1

SA1 was to create a concept for a microdevice capable of *in vitro* axonal compression experiments, in order to simulate the mechanical insult that RGCs have been theorized to experience during glaucoma at the level of the lamina cribrosa. To this end, this work presented the design of the ALD, a device designed to study the effects of mechanical insult applied to the axons of RGCs. The goal of a focal, graded insult was achieved through the inclusion of two functional areas in the device. An array of microchannels was included to separate the axons from the cell bodies of the neurons, to ensure that the mechanical insult applied only contacted the axons. Further, the axonal crushing compartment used a 30 μm wide crushing pad to ensure that the area over which the mechanical insult is applied is repeatable and focal.

6.2.2 Specific Aim 2

SA2 was to develop the means to manufacture the ALD. This aim was achieved through designing and refining the cleanroom process flow to create the master mold for the PDMS replica molding process to make the ALD. Briefly, a set of photomasks were designed for use in the photolithography process, SU-8 formulations for the desired feature height were chosen, and the molds were created through an extensive troubleshooting process to achieve the desired results. The resulting molds were then used to manufacture the ALD.

6.2.3 Specific Aim 3

SA3 was to verify the biocompatibility of the device by maintaining cells in culture for multiple days. This aim was partially met during the time allotted for the project. Initial cell culture experiments were only able to be maintained for approximately 24 hours due to the small volume of medium which was able to be stored in the cell culture reservoir. This issue was overcome by placing the seeded devices in petri dishes flooded by medium, ensuring a large reservoir of medium would be available to the culture. Using this method, cultures of P19 embryonic carcinoma cells were able to be maintained for up to 96 hours, or until confluence was reached. This was confirmed through live /dead staining.

The second aspect to SA3 was to show the efficacy of the microchannels in separating the RGC axons from the soma. This was to be done by seeding differentiated P19 cells in the devices and trying to detect the presence of any axons in microchannels. Differentiated P19 cells were plated in the device, but perhaps due to the relatively low differentiation rate of the P19's, no axons were observed inhabiting microchannels.

6.2.4 Specific Aim 4

SA4, the characterization of the deformation of the PDMS membrane as a function of input pressure, was not competed. The very preliminary, qualitative experiment of observing the PDMS membrane go out of focus as the air bladder was pressurized was a promising result, but lacked the rigorous characterization needed in order to draw correlations between axonal deformation and physiological responses.

APPENDIX A

PHOTOMASK DESIGNS

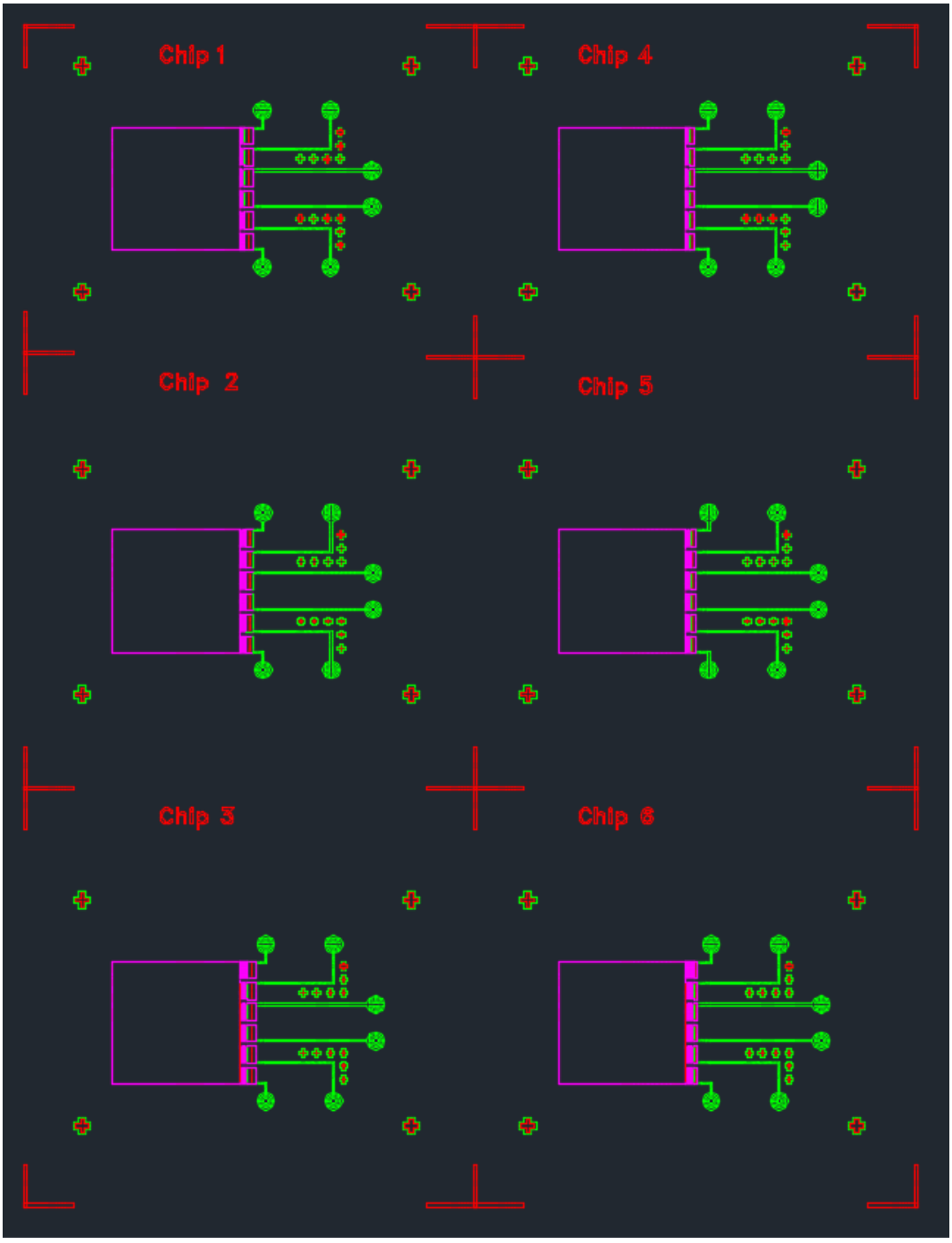

Figure 38: Overlay of all photomask layers

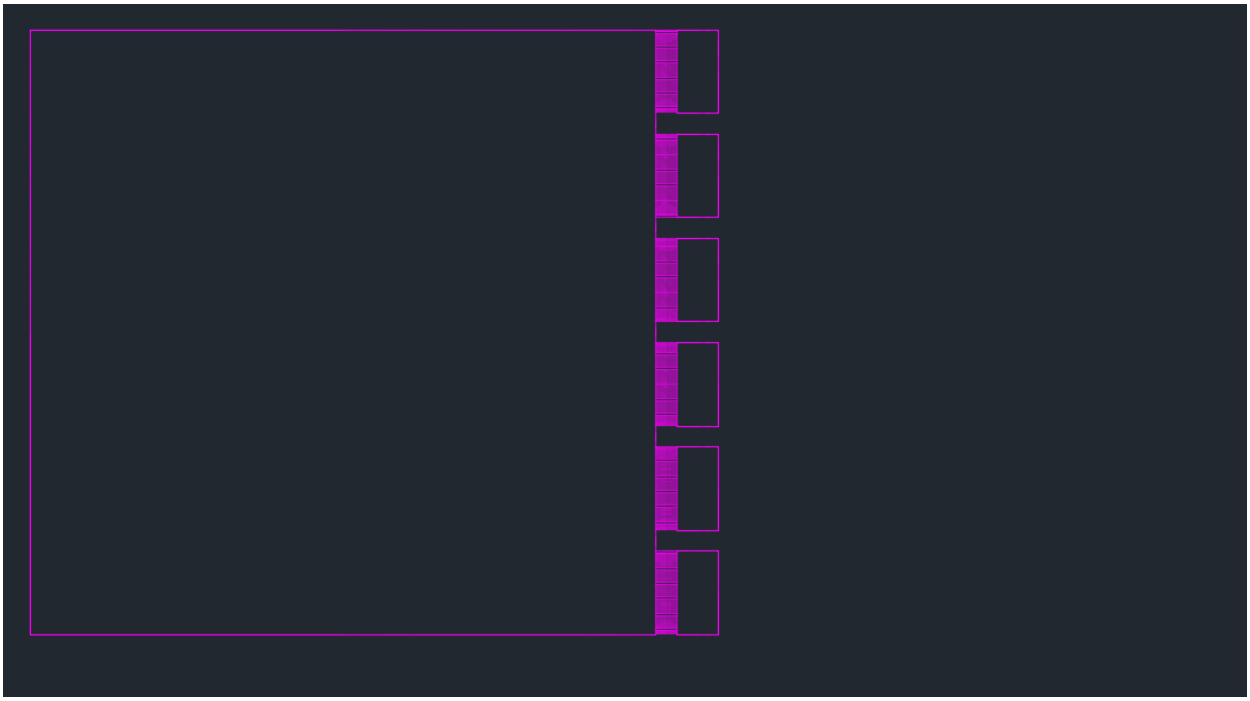

Figure 39: Photomask of the 1st layer of the device

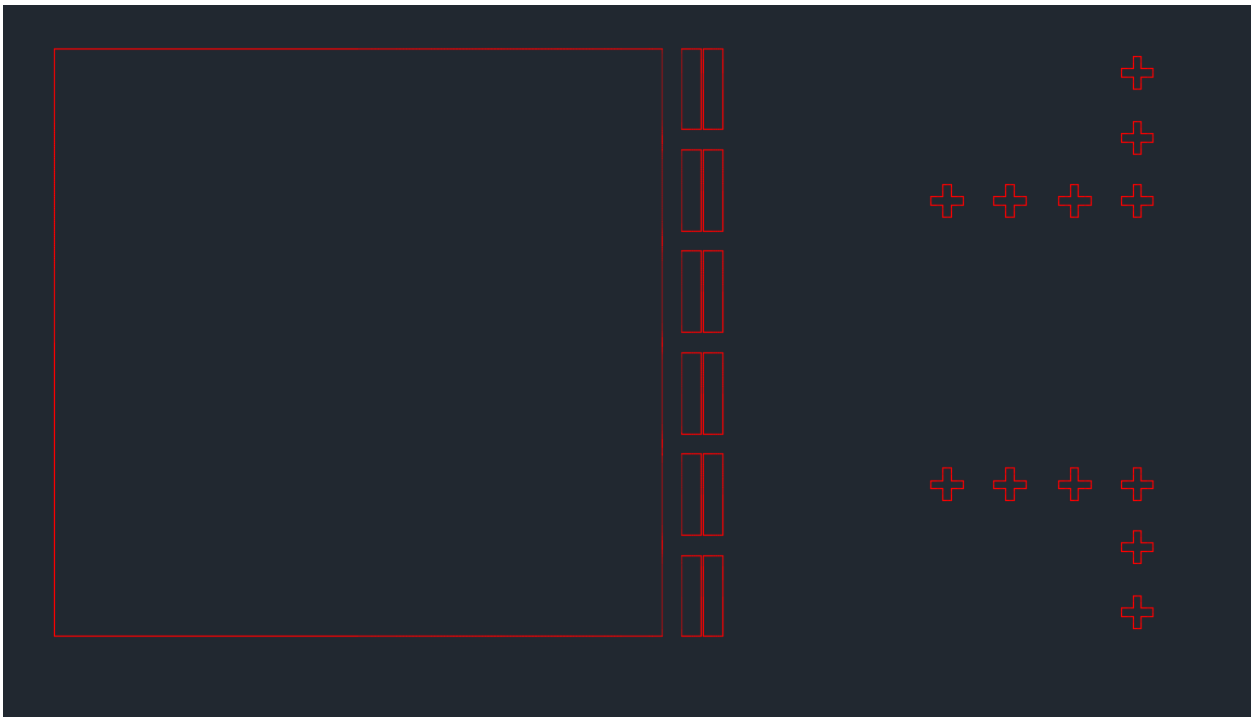

Figure 40: Design of the 2nd layer of the device. Note the alignment crosses to the right to be used in aligning the bottom PDMS layer to the top

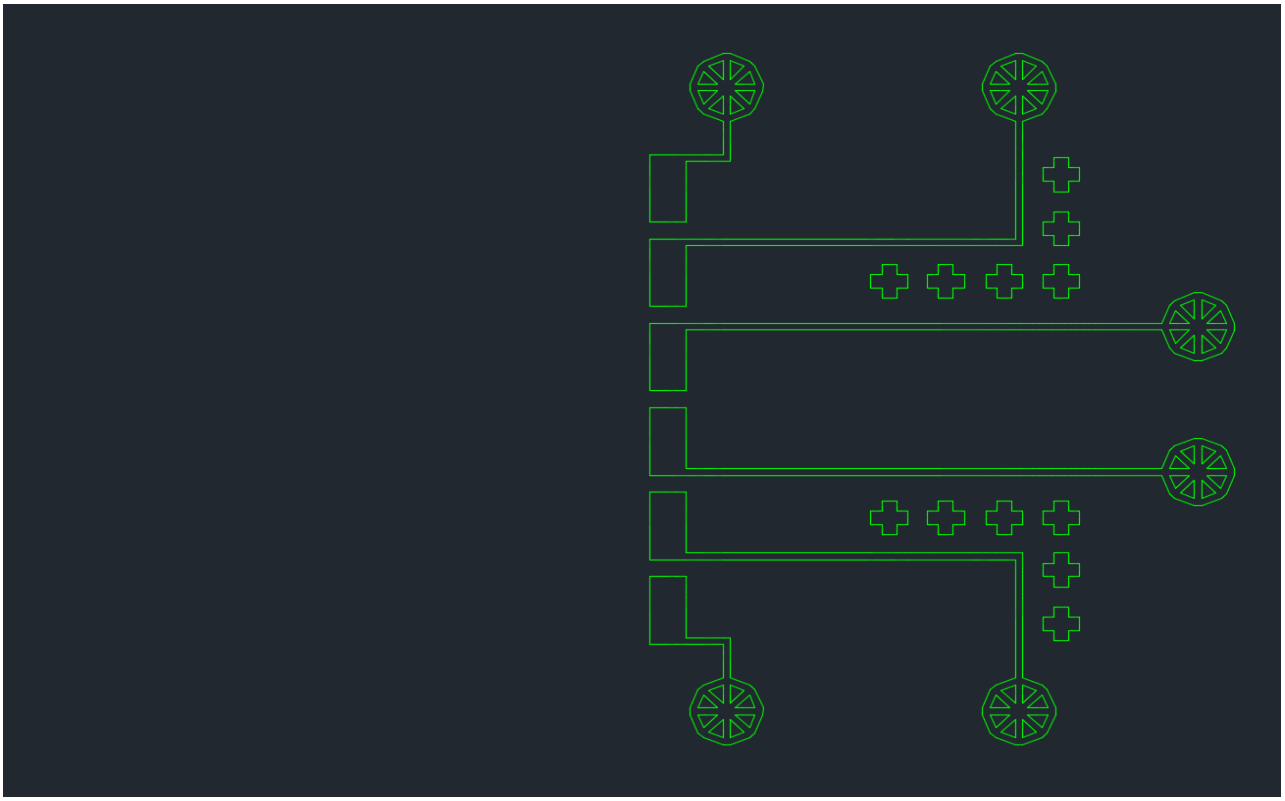

Figure 41: Design of the top layer of the device. Note the alignment crosses to the right

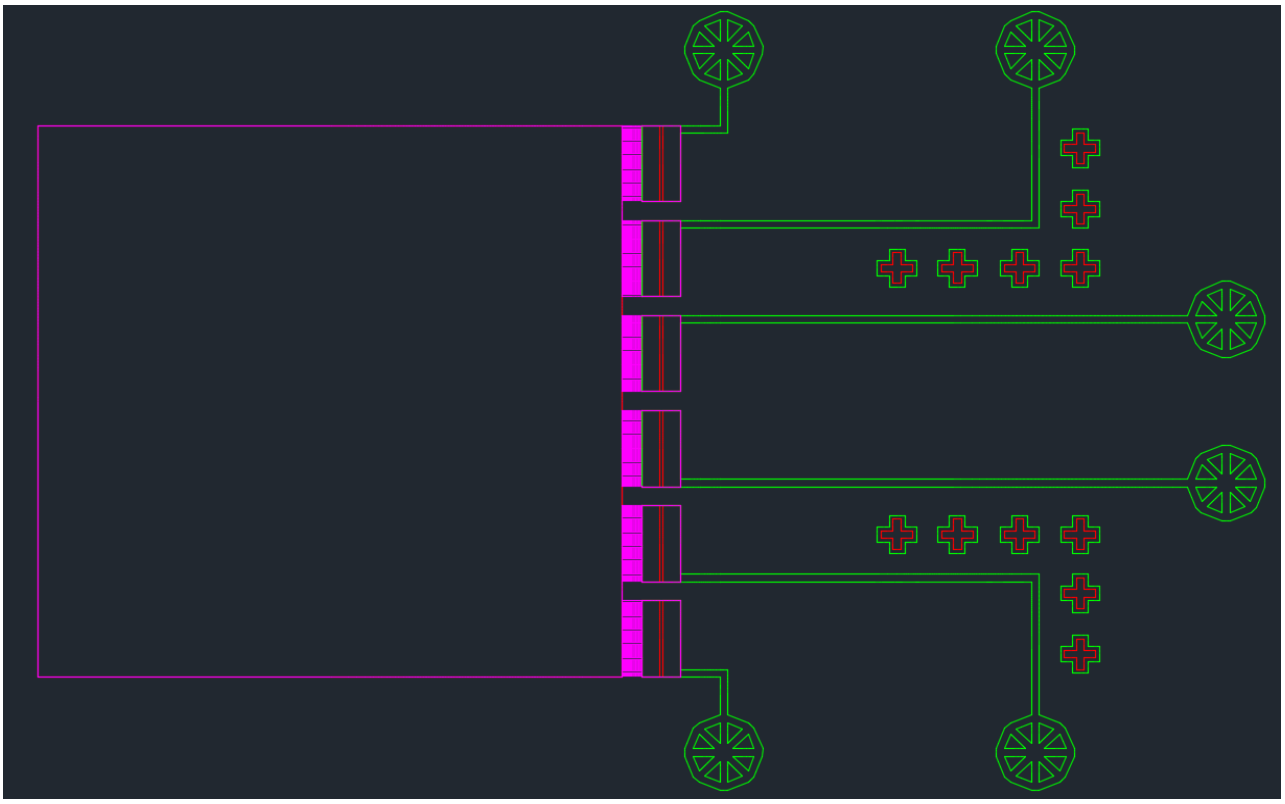

Figure 42: All three photomask designs superimposed to form the whole device design.

Works Cited

[1] H. A. Quigley and A. T. Broman, "The Number of People With Glaucoma Worldwide in 2010 and 2020," *Br. J. Ophthalmol.,* vol. 90, no. 3, pp. 262-267, 2006.

[2] S. Kingman, "Glaucoma is second leading cause of blindness globally," *Bulletin of hte World Health Organization,* pp. 811-890, 2004.

[3] D. B. Rein, P. Zhang, K. E. Wirth, P. Lee, T. J. Hoerger, N. McCall, R. Klein, J. M. Tielsch, S. Vijan and J. Saaddine, "The economic Burden of Major Adult Visual Disorders in the United States," *Arch. Ophthalmol.,* vol. 124, pp. 1754-1760, 2006.

[4] D. J. Calkins and P. J. Horner, "The Cell and Molecular Biology of Glaucoma: Axonopathy and the Brain," *Investigative Ophthalmology & Visual Science,* vol. 53, no. 5, pp. 2482-4, 2012.

[5] H. A. Quigley, G. R. Dunkelberger and W. R. Green, "Retinal ganglion cell atrophy correlated with automated perimetry in human eyes with glaucoma," *Am. J. Ophthalmol.,* vol. 107, pp. 453-464, 1989.

[6] M. R. Hernandez, "The Optic Nerve Head in Glaucoma: Role of Astrocytes in Tissue Remodeling," *Prog. in Ret. and Eye Res.,* vol. 19, no. 3, pp. 297-321, 2000.

[7] "illumination Studios: Enlightening Visualization for Scientific Communication," illumination Studios, 21 October 2011. [Online]. Available: http://illuminationstudios.com/archives/146/eye-anatomy. [Accessed 8 October 2014].

[8] "Sherwood Park Eye Care," 2013. [Online]. Available: http://sherwoodparkeyecare.ca/glaucoma/. [Accessed 8 October 2014].

[9] C. M. Duroga, "Heath and Lifestyle Magazine," 12 12 2009. [Online]. Available: http://healthandlifestylemagazine.wordpress.com/2009/12/12/treating-the-thief-of-sight/. [Accessed 24 9 2014].

[10] A. Sommer, J. M. Tielsch, J. Katz, H. Quigley, J. D. Gottsch, J. Javitt and K. Singh, "Relationship Between Intraocular Pressure and Primary Open Angle Glaucoma Among White and Black Americans. The Baltimore Eye Survey," *Arch. Ophthalmol.,* vol. 109, no. 8, pp. 1090-1095, 1991.

[11] A. Heijl, M. Leske, B. Bengtsson, L. Hyman, B. Gengtsson and M. Hussein, "Reduction of Intraocular Pressure and Glaucoma Progression," *Arch Ophthalmol,* vol. 120, pp. 1268-79, 2002.

[12] I. Campbell, B. Coudrillier and C. R. Ethier, "Biomechanics of the Posterior Eye: A Critical Role in Health and Disease," *Journal of Biomechanical Engineering,* vol. 136, no. 021005, pp. 1-15, 2014.

[13] M. O. Gordon, J. A. Beiser, J. D. Brandt, D. K. Heuer, E. J. Higginbotham, C. A. Johnson, J. L. Keltner, J. P. Miller, R. K. I. Parrish, M. R. Wilson and M. A. Kass, "The Ocular Hypertension Treatment Study: Baseline Factors That Predict the Onset of Primary Open-Angle Glaucoma," *Arch. Ophthalmol.,* vol. 120, no. 6, pp. 714-720, 2002.

[14] R. D. Fechtner and R. N. Weinreb, "Mechanisms of optic nerve damage in primary open angle glaucoma," *Surv. Ophthalmol.,* vol. 39, pp. 23-42, 1994.

[15] E. C. Johnson, L. M. Deppmeier, S. K. Wentzien, I. Hsu and J. C. Morrison, "Chronology of optic nerve head and retinal responses to elevated introcular pressure," *Invest. Ophthalmol. & Vis. Sci.,* vol. 41, no. 2, pp. 431-442, 2000.

[16] A. Llobet, X. Gasull and A. Gual, "Understanding Trabecular Meshwork Physiology: A Key to the Control of Intraocular Pressure?," *News Physiol. Sci.,* vol. 18, pp. 205-209, 1003.

[17] P. G. Watson and R. D. Young, "Scleral structure, organization and disease. A review," *Exp. Eye. Res.,* vol. 78, pp. 609-623, 2004.

[18] A. Elsheikh, B. Geraghty, D. Alhasso, J. Knappett, M. Campanelli and P. Rama, "Regional Variation in the Biomechanical Properties of the human Sclera," *Exp. Eye Res.,* vol. 90, no. 5, pp. 624-633, 2010.

[19] R. D. Young, "The Ultrastructural Organization of Proteoglycans and Collagen in Human and Rabbit Scleral Matrix," *J. Cell Sci.,* vol. 74, pp. 95-104, 1985.

[20] N. A. McBrien, L. M. Cornell and A. Gentle, "Structural and Ultrastructural Changes to the Sclera in a Mammalian Model of High Myopia," *Invest. Ophthalmol. Visual Sci.,* vol. 42, no. 10, pp. 2179-2187, 2001.

[21] J. Morgan, "Circulation and axonal transport in the optic nerve," *Eye,* vol. 18, pp. 1089-1095, 2004.

[22] J. Wang, Z. Medress and B. Barres, "Axon degeneration: molecular mechanisms of a self-destruction pathway," *The Journal of Cell Biology,* vol. 196, no. 1, pp. 7-18, 2012.

[23] H. A. Quigley, "Neuronal death in glaucoma.," *Progress in Retinal and Eye Research,* vol. 18, no. 1, pp. 39-57, 1999.

[24] B. Rydevik, W. G. McLean, J. Sjostrand and G. Lundborg, "Blockage of axonal transport induced by acute, graded compression of the rabbit vagus nerve," *Journal of neurology, neurosurgery, and psychiatry,* vol. 43, no. 8, pp. 690-698, 1980.

[25] I. G. Association, "The Eye: Optic Nerve," [Online]. Available: http://www.glaucoma-association.com/the-eye/optic-nerve.html.

[26] J. B. Jonas, A. M. Schmidt, J. A. Mueller-Bergh, U. M. Schloetzer-Schrehardt and G. O. H. Naumann, "Human Optic Nerve Fiber Count and Optic Disc Size`," *Invest. Ophthalmol. Vis. Sci,* vol. 33, no. 6, pp. 2012-2018, 1992.

[27] H. A. Quigley, E. M. Addicks and W. R. Green, "Optic Nerve Damage in Human Glaucoma," *Arch. Ophthalmol.*, vol. 100, no. 1, pp. 135-146, 1982.

[28] A. R. Elkington, C. B. E. Inman, P. V. Seart and R. O. Weller, "The Structure of the Lamina Cribrosa of the Human Eye: an Immunocytochemical and Electron Microscopiacal Study," *Eye,* vol. 4, pp. 42-57, 1990.

[29] A. J. Bellezza, R. T. Hart and C. F. Burgoyne, "The Optic Nerve Head as a Biomechanical Structure: Initial Finite Element Modeling," *Invest. Ophthalmol. Visual Sci.,* vol. 41, no. 10, pp. 2991-3000, 2000.

[30] A. Fahrny, Strangling neurons: how much can they take?, Master's Thesis, London: Imperial College London, 2012.

[31] J. P. Templeton and E. E. Geisert, "A practical approach to optic nerve crush in the mouse," *Molecular Vision,* vol. 18, pp. 2147-2152, 2012.

[32] J. C. Morrison, C. G. Moore, L. M. Deppmeier, B. G. Gold, C. K. Meshul and E. C. Johnson, "A rat model of chronic pressure-induced optic nerve damage," *Exp Eye Res,* vol. 64, pp. 85-96, 1997.

[33] S. R. Shareef, E. Garcia-Valenzuela, A. Salierno, J. Walsh and S. C. Sharma, "Chronic ocular hypertension following episcleral venous occulusion in rats," *Exp Eye Res,* vol. 61, pp. 379-382, 1995.

[34] D. Gaasterland and C. Kupfer, "Experimental glaucoma in the rhesus monkey," *Invest Ophthalmol,* vol. 13, pp. 455-457, 1974.

[35] T. V. Johnson and S. I. Tomarev, "Rodent models of glaucoma," *2010,* vol. 81, no. 2-3, pp. 349-358, Brain Res Bull.

[36] R. T. Libby, M. G. Anderson, I.-H. Pang, Z. H. Robinson, O. V. Savinova, I. M. Cosma, A. Snow, L. A. Wilson, R. S. Smith, A. F. Clark and S. W. M. John, "Inherited glaucoma in DBA/2J mice: Pertinent disease features for studying the neurodegeneration," *Visual Neuroscience,* vol. 22, pp. 637-648, 2005.

[37] R. T. A. M. G. Libby, I. H. Pang and e. al., "Inherited glaucoma in DBA/2J mice: pertinent disease features for studying the neurodegeneration.," *Visual neuroscience,* vol. 22, pp. 673-648, 2005.

[38] W.-K. Ju, Q. Liu, K. Kim, J. G. Crowston, J. D. Lindsey, N. Agarwal, M. H. Ellisman, G. A. Perkins and R. N. Weinreb, "Elevated Hydrostatic Pressure Triggers Mitochondrial Fission and Decreases Cellular ATP in Differentiated RGC-5 Cells," *Invest. Ophthalmol. Vis. Sci.,* vol. 48, no. 5, pp. 2145-2151, 2007.

[39] M. LaPlaca, D. K. Cullen, J. J. McLoughlin and R. S. Cargill 2nd, "High rate shear strain of three-dimensional neural cell cultures: a new in vitro traumatic brain injury model," *J. Biomech.*, vol. 38, pp. 1093-1105, 2005.

[40] B. Morrison 3rd, D. F. Meaney and T. K. McIntosh, "Mechanical Characterization of an In Vitro Device Designed to Quantitatively Injure Living Brain Tissue," *Ann. Biomed. Eng.*, vol. 26, pp. 381-390, 1998.

[41] D. H. Smith, J. A. Wolf, T. A. Lusardi, V. M.-Y. Lee and D. F. Meaney, "High Tolerance and Delayed Elastic Response of Cultured Axons Dynamic Stretch Injury," *Neurosci*, vol. 19, no. 11, pp. 4264-4269, 1999.

[42] B. J. Pfister, T. P. Weihs, M. Betenbaugh and G. Bao, "An In Vitro Uniaxial Stretch Model for Axonal Injury," *Ann. Biomed. Eng.*, vol. 31, pp. 589-598, 2003.

[43] E. F. Ellis, J. S. Mckinney, K. A. Willoughby, S. Liang and J. T. Povlishock, "A New Model for Rapid Stretch-Induced Injury of Cells in Culture: Characterization of the new Model Using Astrocytes," *J. Neurotrauma*, vol. 12, no. 3, pp. 325-339, 1995.

[44] J.-P. Dolle, B. Morrison III, R. S. Schloss and M. L. Yarmush, "An organotypic uniaxial strain model using microfluidics," *Lab on a Chip*, vol. 13, no. 3, pp. 432-442, 2013.

[45] M. H. Magdesian, S. F. Sanchez, M. Lopez, P. Thostrup, N. Durisic, W. Belkaid, D. Liazoghli, P. Gruetter and D. R. Colman, "Atomic Force Microscopy Reveals Important Differences in Axonal Resistance to Injury," *Biophysical Journal*, vol. 103, no. 3, pp. 405-414, 2012.

[46] D. Sun, J. Qu and T. C. Jakobs, "Reversible Reactivity by Optic Nerve Astrocytes," *Glia*, vol. 61, pp. 1218-1235, 2013.

[47] B. Lorber, A. Guidi, J. W. Fawcett and K. R. Martin, "Activated retinal glia mediated axon regeneration in experimental glaucoma," *Neurobio of Disease*, vol. 45, no. 1, pp. 243-252, 2012.

[48] R. B. Campenot, K. Lund and S. A. Mok, "Production of compartmented cultures of rat sympathetic neurons," *Nature Protocols*, vol. 4, no. 12, pp. 1869-87, 2009.

[49] J. B. Jonas, E. Berenshtein and L. Holbach, "Lamina Cribrosa Thickness and Spatial Relationships between Intraocular Space and Cerebrospinal Fluid Space in Highly Myopic Eyes," *Invest. Ophthalmol. Vis. Sci.*, vol. 45, no. 8, pp. 2660-2665, 2004.

[50] V. Jokinen, P. Sakha, P. Suvanto, C. Rivera, S. Franssila, S. E. Lauri and H. J. Huttunen, "A microfluidic chip for axonal isolation and electrophysiological measurements," *Journal of Neuroscience Methods*, vol. 212, pp. 276-282, 2013.

[51] A. M. Taylor, M. Blurton-Jones, S. W. Rhee, D. H. Cribbs, C. W. Cotman and N. L. Jeon, "A microfluidic culture platform for CNS axonal injury, regeneration and transport," *Nature Methods*, vol. 2, no. 8, pp. 599-606, 2005.

[52] M. A. Unger, H. P. Chou, T. Thorsen, A. Scherer and S. R. Quake, "Monolithic microfabricated valves and pumps by multilayer soft lithography," *Science*, vol. 288, no. 5463, pp. 113-116, 2000.

[53] D. Armani, C. Liu and N. Aluru, "Re-configurable Fluid Circuits by PDMS Elastomer Micromachining," *Micro Electro Mechanical Systems, 1999. MEMS '99. Twelfth IEEE International Conference on,* pp. 222-227, 1999.

[54] C. Livermore and J. Voldman, "6.777J / 2.751J Material Property Database," 19 March 2004. [Online]. Available: http://www.mit.edu/~6.777/matprops/pdms.htm. [Accessed Decem ber 2013].

[55] A. Fluegel, "Statistical Calculation and Development of Glass Properties," 7 Dec. 2007. [Online]. Available: http://glassproperties.com/. [Accessed Dec. 2012].

[56] R. Bernal, P. A. Pullarkat and F. Melo, "Mechanical Properties of Axons," *Phys. Rev. Lett.,* vol. 99, p. 018301, 2007.

[57] R. A. H. El-Mallawany, Tellurite Glasses Handbook: Physical Properties and Data, Boca Raton: CRC Press LLC, 2002.

[58] R. C. Huang and L. Anand, "Non-linear mechanical behavior of the elastomer polydimethylsiloxane (PDMS) used in the manufacture of microfluidic devices," 2005.

[59] S. Hosmane, A. Fournier, R. Wright, L. Rajbhandari, R. Y. I. H. Siddique, K. T. Ramesh, A. Venkatesan and N. Thakor, "Valve-based microfluidic compression platorm: single axon injury and regrowth," *Lab on a Chip,* vol. 11, no. 22, pp. 3888-3895, 2011.

[60] J. C. McDonald and G. M. Whitesides, "Poly(dimethylsiloxane) as a Material for Fabricating Microfluidic Devices," *Accounts of Chemical Research,* vol. 35, no. 7, pp. 491-499, 2002.

[61] M. A. McCord and M. J. Rooks, SPIE Handbook of Microlithography, Micromachining, and Microfabrication, Society of Photo-Optical Instrumentation Engineers, 1997.

[62] Microchem, "SU-8 2000 Permanent Epoxy Negative Photoresist," [Online]. Available: http://www.microchem.com/pdf/SU-82000DataSheet2000_5thru2015Ver4.pdf. [Accessed 15 December 2012].

[63] J. M. Spotts, "Fabrication of PDMS Microfluidic Devices," 15 November 2010. [Online]. Available: https://corefacilities.systemsbiology.net/sites/default/files/MoldMaking_Spotts_2010.pdf. [Accessed December 2012].

[64] P. A. MacPherson and M. W. McBurney, "P19 Embryonal Carcinoma Cells: A Source of Cultured Neurons Amenable to Genetic Manipulation," *METHODS: A Companion to Methods in Enzymology,* vol. 7, pp. 238-252, 1995.

[65] R. M. Gill, R. Slack, M. Kiess and P. A. Kamel, "Regulation of Expression and Activity of Distinct pRB, E2F, D-Type Cyclin, and CKI Family Members during Terminal Differentiation of P19 Cells," *Experimental Cell Research,* vol. 244, pp. 157-170, 1998.

[66] S. Heck, R. Enz, C. Richter-Landsberg and D. Blohm, "Expression of eight metabotropic glutamate receptor subtypes during neuronal differentiation of P19 embryocarcinoma cells: a study by RT-PCR and in situ hybridization," *Developmental Brain Research*, vol. 101, no. 1-2, pp. 81-95, 1997.

[67] P. K. Datta, "Murine Teratocarcinoma-Derived Neuronal Cultures," *Methods Mol. Bio.*, pp. 35-44, 2013.

[68] E. Barber, *Studies on retroviral vectors to controllably express genes in neuronal like cells*, Galway: National University of Ireland., 2005.

[69] C. Bowd, L. Sangwill, C. Berry, E. Blumenthal, C. Vasile, C. Sanchez-Galeana, C. Bosworth, P. Samples and R. Weinreb, "Detecting Early Glaucoma by Assessment of Retinal Nerve Fiber Layer Thickness and Visual Function," *Invest. Ophthalmol. Vis. Sci.*, vol. 42, no. 9, pp. 1993-2003, 2001.

[70] M. Civan, The Eye's Aqueous Humor, Edition 2, San Diego: Elsevier, Inc., 2008.

[71] R. Grytz, G. Meschke and J. B. Jonas, "The Collagen Fibril Architecture in the Lamina Cribrosa and Peripapillary Sclera Predicted by a Computational Remodeling Approach," *Biomech. Model. Mechanobiol.*, vol. 10, no. 3, pp. 371-382, 2011.

[72] I. A. Sigal, J. G. Flanagan and C. R. Ethier, "Factors Influencing Optic Nerve Head Biomechanics," *Invest. Ophthalmol. Visual Sci.*, vol. 46, no. 11, pp. 4189-4199, 2005.

[73] J. K. Pijanka, B. Coudrillier, K. Ziegler, T. Sorensen, K. M. Meek, T. D. Nguyen, H. A. Quigley and C. Boote, "Quantitative Mapping of Collagen Fiber Orientation in Non-Glaucoma and Glaucoma POsterior Human Sclerae," *Invest. Ophthalmol. Visual Sci.*, vol. 32, no. 8, pp. 2244-2258, 2012.

[75] H. Gray, Anatomy of the Human Body, Philadelphia: Lea & Febiger, 1918.